

## RESEARCH ARTICLE

Loss of *Katnal2* leads to ependymal ciliary hyperfunction and autism-related phenotypes in mice

Ryeonghwa Kang<sup>1,2</sup>, Kyungdeok Kim<sup>2</sup>, Yewon Jung<sup>1</sup>, Sang-Han Choi<sup>3,4</sup>, Chanhee Lee<sup>3</sup>, Geun Ho Im<sup>3</sup>, Miram Shin<sup>5</sup>, Kwangmin Ryu<sup>1</sup>, Subin Choi<sup>5</sup>, Esther Yang<sup>6</sup>, Wangyong Shin<sup>2</sup>, Seungjoon Lee<sup>2</sup>, Suho Lee<sup>2</sup>, Zachary Papadopoulos<sup>7</sup>, Ji Hoon Ahn<sup>8</sup>, Gou Young Koh<sup>8</sup>, Jonathan Kipnis<sup>7,9,10</sup>, Hyojin Kang<sup>11</sup>, Hyun Kim<sup>6</sup>, Won-Ki Cho<sup>1</sup>, Soochul Park<sup>5</sup>, Seong-Gi Kim<sup>3,4</sup>, Eunjoon Kim<sup>1,2\*</sup>

**1** Department of Biological Sciences, Korea Advanced Institute of Science and Technology (KAIST), Daejeon, Korea, **2** Center for Synaptic Brain Dysfunctions, Institute for Basic Science (IBS), Daejeon, Korea, **3** Center for Neuroscience Imaging Research, Institute for Basic Science (IBS), Suwon, Korea, **4** Department of Biomedical Engineering, Sungkyunkwan University, Suwon, Korea, **5** Department of Biological Sciences, Sookmyung Women's University, Seoul, Korea, **6** Department of Anatomy, Biomedical Sciences, College of Medicine, Korea University, Seoul, Korea, **7** Neuroscience Graduate Program, School of Medicine, Washington University in St. Louis, St. Louis, Missouri, United States of America, **8** Center for Vascular Research, Institute for Basic Science (IBS), Daejeon, Korea, **9** Brain Immunology and Glia (BIG) Center, Washington University in St. Louis, St. Louis, Missouri, United States of America, **10** Department of Pathology and Immunology, School of Medicine, Washington University in St. Louis, St. Louis, Missouri, United States of America, **11** Division of National Supercomputing, Korea Institute of Science and Technology Information (KISTI), Daejeon, Korea

☯ These authors contributed equally to this work.

\* [kime@kaist.ac.kr](mailto:kime@kaist.ac.kr)



OPEN ACCESS

**Citation:** Kang R, Kim K, Jung Y, Choi S-H, Lee C, Im GH, et al. (2024) Loss of *Katnal2* leads to ependymal ciliary hyperfunction and autism-related phenotypes in mice. *PLoS Biol* 22(5): e3002596. <https://doi.org/10.1371/journal.pbio.3002596>

**Academic Editor:** Richard Daneman, UCSD, UNITED STATES

**Received:** March 13, 2023

**Accepted:** March 21, 2024

**Published:** May 8, 2024

**Peer Review History:** PLOS recognizes the benefits of transparency in the peer review process; therefore, we enable the publication of all of the content of peer review and author responses alongside final, published articles. The editorial history of this article is available here: <https://doi.org/10.1371/journal.pbio.3002596>

**Copyright:** © 2024 Kang et al. This is an open access article distributed under the terms of the [Creative Commons Attribution License](https://creativecommons.org/licenses/by/4.0/), which permits unrestricted use, distribution, and reproduction in any medium, provided the original author and source are credited.

**Data Availability Statement:** Raw RNA-Seq data are available as GSE219228 at Gene Expression Omnibus (GEO), National Center for Biotechnology Information (NCBI). The custom MATLAB code

## Abstract

Autism spectrum disorders (ASD) frequently accompany macrocephaly, which often involves hydrocephalic enlargement of brain ventricles. *Katnal2* is a microtubule-regulatory protein strongly linked to ASD, but it remains unclear whether *Katnal2* knockout (KO) in mice leads to microtubule- and ASD-related molecular, synaptic, brain, and behavioral phenotypes. We found that *Katnal2*-KO mice display ASD-like social communication deficits and age-dependent progressive ventricular enlargements. The latter involves increased length and beating frequency of motile cilia on ependymal cells lining ventricles. *Katnal2*-KO hippocampal neurons surrounded by enlarged lateral ventricles show progressive synaptic deficits that correlate with ASD-like transcriptomic changes involving synaptic gene down-regulation. Importantly, early postnatal *Katnal2* re-expression prevents ciliary, ventricular, and behavioral phenotypes in *Katnal2*-KO adults, suggesting a causal relationship and a potential treatment. Therefore, *Katnal2* negatively regulates ependymal ciliary function and its deletion in mice leads to ependymal ciliary hyperfunction and hydrocephalus accompanying ASD-related behavioral, synaptic, and transcriptomic changes.

used for the analysis is available in <https://github.com/sjleen/Cilia-stroke-analysis>.

**Funding:** This work was supported by the National Research Foundation of Korea grants RS-2023-00272290 (to HK), 2022M3A9B6082673 (to WKC), and NRF-2021R1A2C3011919 (to SP) funded by the Korean government and the Institute for Basic Science (IBS) (IBS-R015-D1 to SGK and IBS-R002-D1 to EK). The funders had no role in study design, data collection and analysis, decision to publish, or preparation of the manuscript.

**Competing interests:** The authors have declared that no competing interests exist.

**Abbreviations:** ASD, autism spectrum disorder; AUC, areas under the curve; BP, biological process; CBV, cerebral blood volume; CC, cellular component; CSF, cerebrospinal fluid; DEG, differentially expressed gene; EPSC, excitatory postsynaptic current; FDR, false discovery rate; fps, frames per second; GE-EPI, gradient-echo echo-planar image; GO, gene ontology; GSEA, gene set enrichment analysis; ICP, intracranial pressure; KO, knockout; LW, lateral wall; MF, molecular function; MRI, magnetic resonance imaging; MT, microtubule; NES, normalized enrichment score; PBS, phosphate-buffered saline; PCR, polymerase chain reaction; SEM, scanning electron microscopy; USV, ultrasonic vocalization; WT, wild type.

## Introduction

Autism spectrum disorders (ASD) represent a neurodevelopmental disorder characterized by social deficits and repetitive behaviors. Macrocephaly with increased brain size is frequently associated with ASD and neurodevelopmental disorders [1,2]. Macrocephaly in ASD can involve hydrocephalus [3,4], wherein ventricular cavities containing the cerebrospinal fluid (CSF) are abnormally enlarged [5,6]. Hydrocephalus can arise from various causes; among them are impairments in the circulation of CSF across ventricular structures, which is facilitated by the synchronous beating of the motile cilia belonging to ependymal cells lining ventricular walls [7–11]. Although primary and motile cilia and related genes have been implicated in hydrocephalus [9,10,12], it remains unknown whether ciliopathies could underlie ASD-related hydrocephalus and macrocephaly. Furthermore, previous studies have mostly focused on conditions in which the ependymal cilia are malfunctioning, despite the possibility that an increased ependymal ciliary function can also lead to hydrocephalus.

Microtubules (MTs) regulate various cellular morphologies and functions, including MT-dependent cellular motility and protein transport [13]. *Katnal2* localizes to MT-based structures, such as primary and motile cilia; it is thought to regulate MTs, based on its structural similarity to the known MT-severing proteins, *Katna1* and *Katnal1*, although direct MT-severing activity has not been observed [14–17]. Previous studies on *in vivo* functions of *Katnal2* have mainly focused on how developmental processes are affected by *Katnal2* deletion or knockdown. *Katnal2* knockout (KO) in mice inhibits MT-related spermatogenic processes (i.e., spermiogenesis) [18,19]. *Katnal2* knockdown in the developing *Xenopus* embryo suppresses epithelial cell ciliogenesis and telencephalic development [14]. *Katnal2* KO in zebrafish leads to delayed embryonic development and abnormal social behaviors [20]. An acute Crispr-mediated *Katnal2* KO in the neonatal mouse hippocampus suppresses the dendritic growth of dentate granule cells [21]. Clinically, *Katnal2* has been strongly implicated in ASD [22–29]. However, it remains unclear whether and how *Katnal2* KO in mice leads to ASD-related behavioral, brain, synaptic, and molecular/cellular phenotypes.

We found that mice lacking *Katnal2* proteins, which are highly expressed in ependymal cells lining the brain ventricles, show social communication deficits and age-dependent progressive enlargements of brain ventricles (ventriculomegaly). These changes involved abnormal lengthening and excessive beating of motile cilia on ependymal cells lining ventricles. These changes accompanied impaired synaptic functions involving ASD-like transcriptomic changes and synaptic gene down-regulations. Importantly, early postnatal re-expression of *Katnal2* prevented the ventricular and behavioral phenotypes in adult mutant mice. Therefore, *Katnal2* negatively regulates ependymal ciliary development and function, and *Katnal2* KO can lead to ASD-related behavioral, ventricular, synaptic, and transcriptomic changes. More generally, our study demonstrates that hydrocephalus can be caused by both limited and excessive ependymal ciliary functions.

## Results

### Abnormal social communication and mounting in *Katnal2*-KO mice

To investigate *in vivo* functions of *Katnal2*, which is a MT-related protein that has been strongly implicated in ASD (S1A Fig), we used a mouse embryonic cell line (EUCOMM, MAE-4330) to generate *Katnal2*-KO mice carrying a frame-shifting homozygous deletion of exon 3 (S1B and S1C Fig). *Katnal2*-KO mice lacked detectable *Katnal2* protein in homozygotes and showed normal mendelian ratios and body weights (S1D and S1E Fig). *Katnal2*-KO brains were largely normal in cortical layer structures, as assessed using the markers NeuN

(neurons), *Cux1* (layer 2/3), and *Foxp2* (layer 6) (**S1F and S1G Fig**). *Katnal2* KO did not affect dendritic morphology, which is strongly affected by microtubule structures, as determined by the Sholl analysis of CA1 hippocampal neurons in *Katnal2*-KO mice crossed with *Thy1*-EGFP mice [30] (**S1H Fig**). In addition, *Katnal2* KO did not affect the length of the primary cilia, a microtubule-based structure protruding from the cell surface and is implicated in neuronal signaling [31], in cultured hippocampal neurons, as determined by immunostaining for *Arl13b* and *NeuN*, markers of primary cilia and neurons, respectively (**S1I Fig**).

Given that *Katnal2* is associated with ASD, we first tested if *Katnal2*-KO mice show autistic-like behavioral deficits. *Katnal2*-KO mice showed normal social approach and social novelty recognition in the three-chamber test, as compared with wild-type (WT) mice (**S2A Fig and S1 Data** [statistical details and numerical data]). *Katnal2*-KO and WT mice did not display any genotype-related difference in the direct social interaction test (**S2B Fig**). *Katnal2*-KO mice also acted normally in unidirectional direct social interactions involving a stranger mouse of a different coat color (**S2C Fig**).

In tests measuring social communication through ultrasonic vocalizations (USVs), an adult male *Katnal2*-KO mouse emitted courtship USVs of increased frequency and duration upon encounter with a female stranger mouse (**S2D Fig**). To better understand this change, we analyzed direct social interactions occurring in the courtship arena. We found no genotype-related difference in uni- or bidirectional social interactions (male-to-female, female-to-male, and reciprocal) (**S2E Fig**). Intriguingly, however, male *Katnal2*-KO mice exhibited reduced mounting success (**S2F Fig**). *Katnal2*-KO mice displayed normal repetitive self-grooming (**S2G Fig**).

In other behavioral tests, *Katnal2*-KO mice showed normal levels of locomotor activity in the open-field test and normal levels of anxiety-like behaviors in the open-field, elevated-plus maze, and light-dark tests (**S3A–S3C Fig**). *Katnal2*-KO mice showed normal auditory function in the acoustic startle test and normal motor coordination in the rotarod test (**S3D and S3E Fig**). Lastly, *Katnal2*-KO mice performed normally in learning and memory tests, including the Morris water maze, novel object-recognition, and contextual-fear conditioning tests (**S3F–S3H Fig**). These results suggest that *Katnal2*-KO mice show selective abnormalities in social communication at adult stages.

### Progressive ventricular enlargements in *Katnal2*-KO mice

While performing the slice-staining experiments mentioned above, we noticed that the ventricles in *Katnal2*-KO brains were abnormally enlarged, suggestive of hydrocephalus. We thus quantitatively compared the brain areas and ventricular sizes of WT and *Katnal2*-KO brains at 3 different postnatal stages (P7, P28, and P70).

Pronounced ventricular enlargements in the two lateral ventricles of *Katnal2*-KO brains were observed at P28 and P70 (**Fig 1A–1C**). Some mutant mice (<10%) showed visually detectable macrocephaly with abnormal head shapes at approximately P28 (**Fig 1B**) and tended to die at approximately P30–40. Total brain areas in coronal slices were moderately increased at P70 but not at P28 in *Katnal2*-KO mice (**Fig 1A and 1C**). At P7, lateral ventricular enlargements were moderate compared with those at P28 and P70 (**S4A Fig**).

Magnetic resonance imaging (MRI) analysis revealed similar ventricular enlargements in the volumes of lateral ventricles among *Katnal2*-KO mice (3 months) (**Fig 1D**). In contrast, the intracranial volumes of mutant mice (encompassing all ventricular and non-ventricular brain regions) remained largely unchanged, with very moderate increases in selective brain regions (**Figs 1D and S4B**). These results collectively suggest that *Katnal2* KO in mice leads to

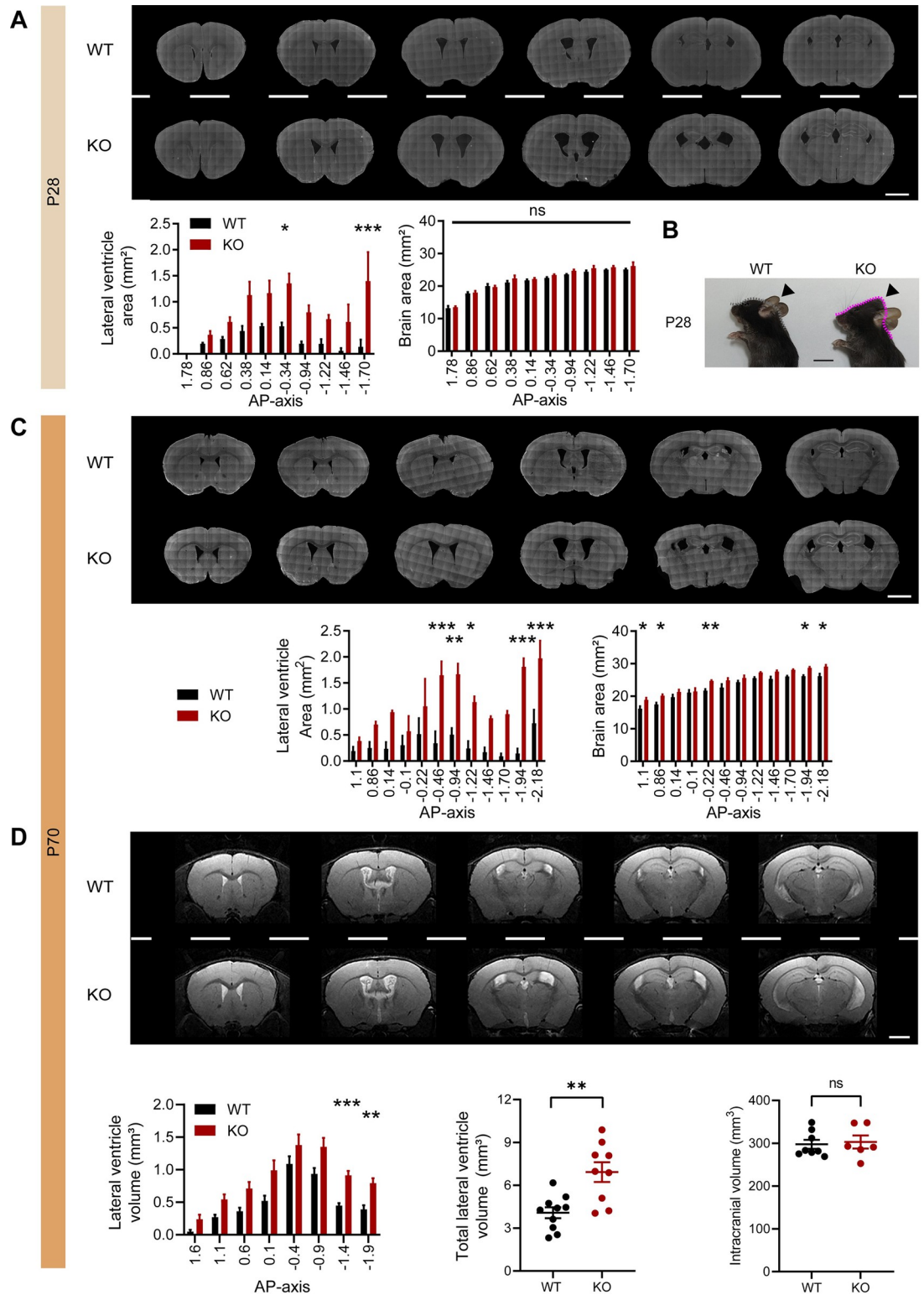


**Fig 1. Age-dependent progressive ventricular enlargements in *Katnal2*-KO mice.** (A–C) Increased areas of lateral ventricles in *Katnal2*-KO mice at P28 and P70, as shown by area measurements derived from coronal brain slices. Note that brain areas are moderately increased at P70 but not at P28. The image in (B) shows an example of the visually detectable abnormalities in the external regions of the head in some (<10%) mice (P28), likely reflecting severe hydrocephalus. AP axis, anterior-posterior axis. Scale bar, 2 mm. (*n* = 3 mice [WT-P28], 3 [KO-P28]; 3 [WT-P70], 3 [KO-P70], two-way RM-ANOVA with Sidak’s test). (D)

Increased volumes of lateral ventricles with unaltered intracranial volumes (total brain volume encompassing ventricular + non-ventricular brain regional volumes) in *Katnal2*-KO mice (3 months), as shown by MRI volumetric analyses. Scale bar, 2 mm. ( $n = 8$  mice [WT-intracranial volume], 6 [KO-intracranial volume], Student's  $t$  test;  $n = 10$  mice [WT-lateral ventricle volume], 9 [KO-lateral ventricle volume], two-way RM-ANOVA with Sidak's test). Data values represent means  $\pm$  SEM. Significance is indicated as \* ( $<0.05$ ), \*\* ( $<0.01$ ), \*\*\* ( $<0.001$ ), or ns (not significant). Statistical results and numerical data values can be found in [S1 Data](#). KO, knockout; MRI, magnetic resonance imaging; WT, wild type.

<https://doi.org/10.1371/journal.pbio.3002596.g001>

age-dependent and progressive ventricular enlargements with moderate effects on total brain areas and that severe macrocephaly is observed in some cases.

### **Katnal2 localization in ventricular ependymal cells**

The hydrocephalus observed in *Katnal2*-KO mice may involve impaired circulation of the CSF through the ventricular system. We thus tested if *Katnal2* proteins are distributed to ventricle-related structures of the mouse brain using X-gal staining of brain slices from *Katnal2*-KO mice expressing *Katnal2*- $\beta$ -galactosidase fusion proteins ([S1B Fig](#)).

*Katnal2* signals at P21 were detected in multiple brain regions, including ventricle-related regions, such as the linings of the lateral and third ventricles where ependymal cells are located ([Figs 2A](#) and [S5A](#)). *Katnal2* was also detected in the choroid plexus, a CSF-producing vascular structure in ventricles, as well as in other brain regions, such as the septum, hippocampus, amygdala, and hypothalamus. At P56, *Katnal2* was additionally detected in cortical layers ([S5B Fig](#)).

In a combined fluorescence in situ hybridization and immunofluorescence staining, *Katnal2* mRNAs colocalized with S100 (ependymal cell marker) and acetylated  $\beta$ -tubulin (cilia marker) in the ependymal cells lining lateral/third ventricles ([Fig 2B and 2D](#)). *Katnal2* mRNAs also colocalized with FoxJ1 (choroid plexus marker) in the choroid plexus of lateral/third ventricles ([Fig 2C and 2E](#)). These results indicate that *Katnal2* is expressed in the choroid plexus and ependymal cells, which regulate CSF production and CSF circulation, respectively, in the ventricular system [7,32].

### **Lengthened ependymal cilia and increased ciliary beating function and frequency in the *Katnal2*-KO brain**

*Katnal2* is an MT-related protein. Notably, ependymal cilia comprise an MT-based 9+2 axonemal structure, and hydrocephalus can be caused by ciliary impairments [9,33]. We thus tested whether *Katnal2* KO leads to altered ependymal ciliary structures in *Katnal2*-KO mice using scanning electron microscopy (SEM).

SEM analysis indicated that the ciliary length was abnormally increased in *Katnal2*-KO mice ([Figs 3A, 3B, and S6](#)), suggesting that *Katnal2* negatively regulates the length of the axonemal structure in ependymal cilia.

To determine functional abnormalities in *Katnal2*-KO ependymal cilia, we first measured the flow rate of fluorescent beads moving across lateral ventricular walls in a whole-mount en face brain preparation ([Fig 3C](#)). Time-lapse imaging indicated that there are significant increases in the flow rates in the three tested flow pathways ([Fig 3D–3G](#)). In a control experiment, the bead flow rate was substantially decreased in the presence of pneumolysin ([Fig 3H](#)), a pore-forming pneumococcal toxin known to suppress ependymal ciliary beating and CSF flow in an irreversible manner [34–37]. These results suggested that *Katnal2* KO enhanced ependymal ciliary function.

We next measured ependymal ciliary beating frequency in brain slices using a high-speed (approximately 1,000 frames/sec) camera and video clip analysis ([Fig 3I and S1 Movie](#)).

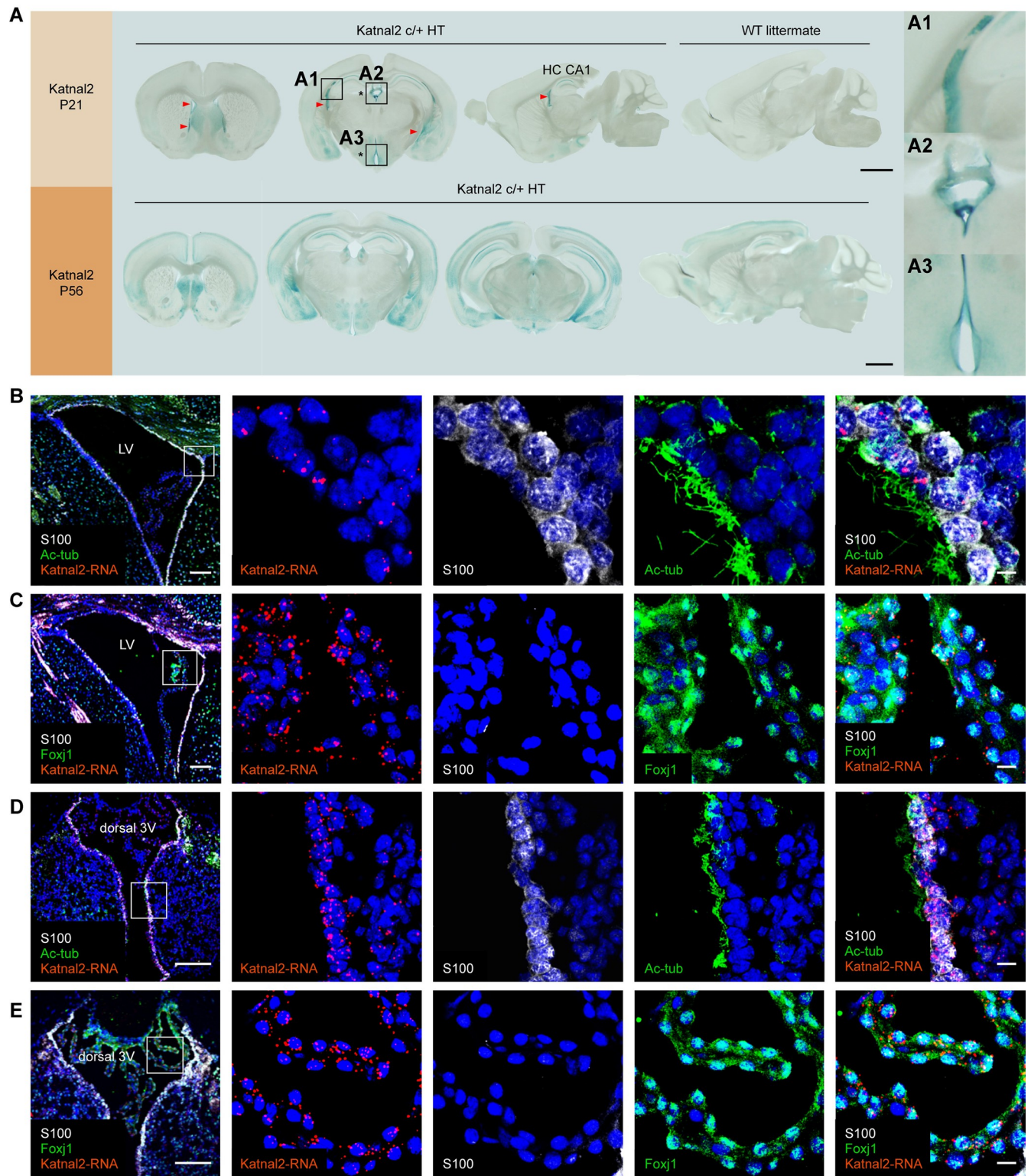


**Fig 2. *Katnal2* localization in ventricular ependymal cells.** (A) Distribution patterns of *Katnal2* proteins in ventricle-related structures (ventricles [arrowheads] and choroid plexus [the bottom structure in enlarged inset a2]) in the mouse brain, as revealed by X-gal staining of *Katnal2*- $\beta$ -galactosidase fusion proteins expressed in *Katnal2*-KO mice with the  $\beta$ -geo cassette left intact (P21 and P56). Note that *Katnal2* is additionally detected in cortical layers at P56 but not at P21. Enlarged insets: a1, lateral ventricle; a2, dorsal third ventricle; a3, ventral third ventricle. See also S5 Fig for additional images. Scale bar, 1 mm. (B–E) Localizations of *Katnal2* mRNAs in the ependymal cells and choroid plexus in the lateral ventricles (b, c; LV) and dorsal third ventricles (d, e;

D3V) of WT mice (P56), as shown by combined fluorescence in situ hybridization for *Katnal2* mRNAs and immunofluorescence staining for S100 (ependymal cell marker), acetylated  $\beta$ -tubulin (cilia marker; Ac-tub), and FoxJ1 (choroid plexus marker). Scale bar, 100  $\mu$ m (left) and 10  $\mu$ m (magnified images, right). KO, knockout; WT, wild type.

<https://doi.org/10.1371/journal.pbio.3002596.g002>

Intriguingly, *Katnal2*-KO cilia showed an increased ciliary beating frequency in lateral ventricles (Fig 3I). This increase in beating frequency, together with the lengthened cilia, suggests that *Katnal2* KO may enhance ependymal ciliary function, leading to a stronger propulsion of CSF (Fig 3J).

Increased CSF propulsion would exert greater hydraulic turbulences on downstream CSF channels. Indeed, we found that the flow rates of CSF in the cerebral aqueduct, which links the third and fourth ventricles, was increased in the brains of anesthetized *Katnal2*-KO mice, as measured by MRI (Fig 3K). However, the intracranial pressure was not changed in the brains of *Katnal2*-KO mice (Fig 3L), suggestive of a counteraction between increased hydraulic turbulence and increased ventricular volume reached at an equilibrium. We performed these experiments mainly using *Katnal2*-KO mice at ages >P28 because ependymal ciliary maturation is established at around P21–28 [38–40].

These results collectively suggest that *Katnal2* KO enlengthens ependymal ciliary length and enhances ciliary beating function and frequency, leading to increased CSF propelling down the stream.

### Progressive synaptic deficits in the *Katnal2*-KO hippocampus

Hydrocephalus can compress brain parenchyma, including perivascular spaces, and cause pathophysiological changes in compressed neurons and axons [41,42], as exemplified by impaired synaptic plasticity in animal models of chronic hydrocephalus [43]. We thus measured cerebral blood volumes (CBVs) in the *Katnal2*-KO brain (Fig 4A–4D) and synaptic transmission and plasticity (Fig 4E–4N) in the *Katnal2*-KO hippocampus, a brain region surrounded by the enlarged lateral ventricles.

CBV-weighted signals, measured by  $T_2^*$ -weighted single-shot gradient-echo echo-planar images (GE-EPI) combined with acute hypoxic nitrogen stimulus [44], were decreased in various brain regions, including the hippocampus (Figs 4A–4D and S7A). In contrast, CBV-weighted signals around the choroid plexus were unaffected (S7B and S7C Fig), suggesting that CSF production, relying on the blood flow to the choroid plexus [45], was not changed. In addition, immunoblot analysis of choroid plexus lysates indicated the lack of genotype difference in the levels of proteins known to regulate CSF secretion such as ion co-transporters ( $\text{Na}^+$ - $\text{K}^+$ -ATPase and anion exchanger 2/AE2; marking apical and basolateral epithelial membranes, respectively) and the water channel aquaporin-1 (AQP1) [46,47] (S7D Fig) further suggesting that CSF production is not changed in *Katnal2*-KO mice. There were no changes in the drainage of CSF from the brain to the lymph nodes outside the brain, as measured by the signals of fluorescent ovalbumin injected into lateral ventricles and retrieved in the deep cervical lymph nodes (S7E and S7F Fig).

Measurements of hippocampal synaptic functions in juvenile (P20–33) *Katnal2*-KO mice indicated normal long-term potentiation induced by theta-burst stimulation (TBS-LTP) at Schaffer collateral-CA1 (SC-CA1) synapses (Fig 4E). In addition, there was no change in basal synaptic transmission (AMPA receptor-mediated excitatory postsynaptic currents [EPSCs]), presynaptic release (paired-pulse facilitation), or the NMDA/AMPA ratio (ratio of NMDA receptor- and AMPA receptor-mediated EPSCs) (Fig 4F–4H). Neuronal excitability in CA1 neurons was also normal, as shown by the input-firing curve (Fig 4I).

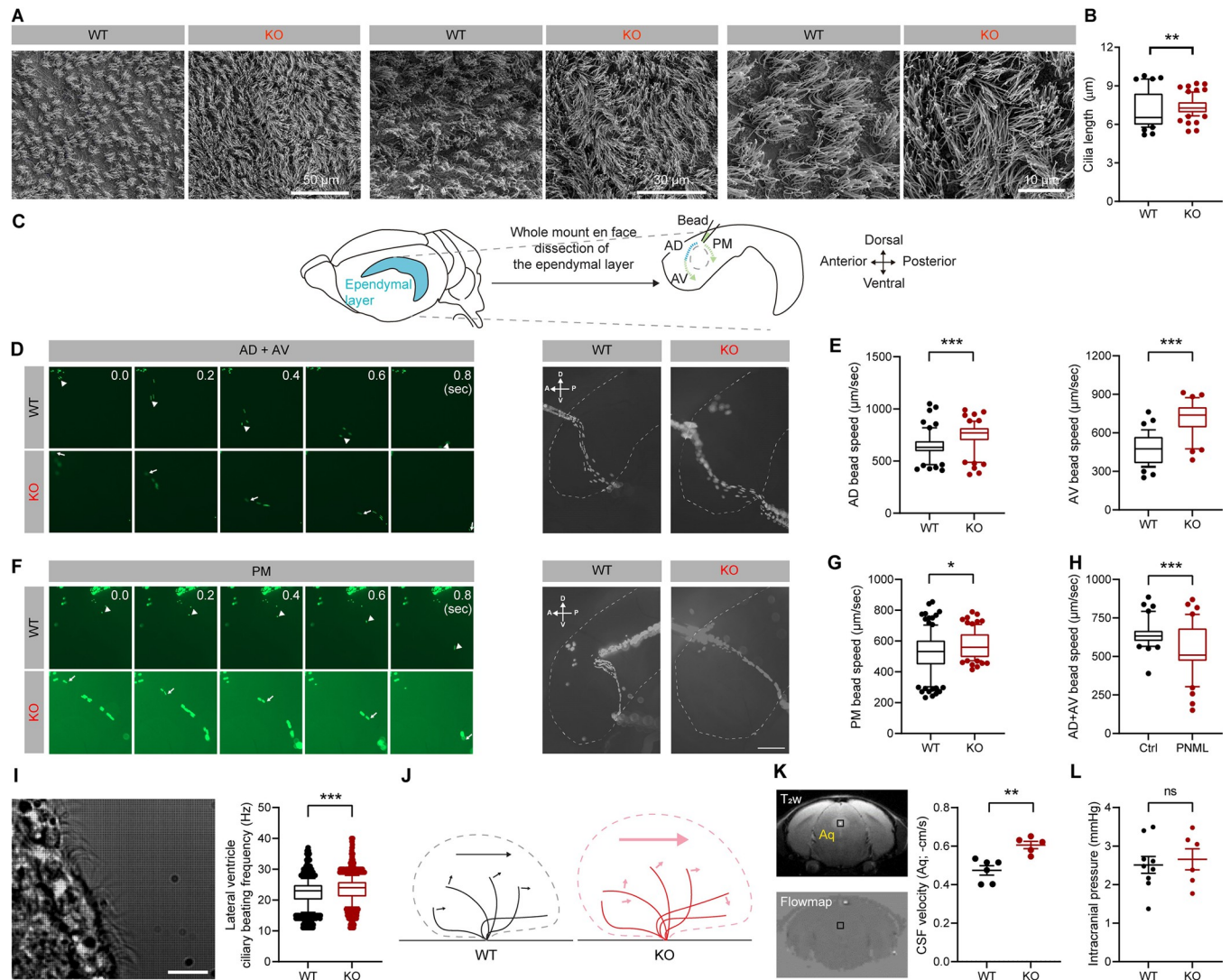


**Fig 3. Lengthened ependymal cilia and increased ciliary beating function and frequency in the *Katnal2*-KO brain.** (A and B) Increased length of ependymal motile cilia in *Katnal2*-KO mice (P28–33), as determined from SEM images of lateral ventricular walls. ( $n = 42$  cilia from 6 images from 6 mice [WT], 77, 11, 11 [KO], Mann–Whitney test). (C–H) Enhanced ependymal ciliary function in *Katnal2*-KO mice (P31–40), as shown by bead flow assays using the ependymal tissue of lateral ventricular walls. (C) Schematic diagram showing the movement of fluorescent beads on live lateral ventricular walls. The bead flow follows the anterior-dorsal (AD), anterior-ventral (AV), or posterior-medial (PM) direction around the adhesion area. (D and F) High-speed video imaging analysis of each fluorescent bead at different time points. The movement of each bead was marked by arrowheads. Five consecutive frames taken by 200 msec intervals were merged into a single image. Scale bar, 200  $\mu\text{m}$ . (E and G) Quantification of the speed of microbeads. ( $n = 60$  beads from 4 mice [WT-AD], 39, 4 [WT-AV], 62, 4 [KO-AD], 33, 4 [KO-AV], 116, 4 [WT-PM], and 82, 4 [KO-PM], Student's *t*-test [AV bead speed], Mann–Whitney test [AD bead speed, PM bead speed]). (H) A decreased speed of microbeads in AD + AV regions after a 10-min pretreatment of brain slices with pneumolysin (PNML; 0.5  $\mu\text{g}/\text{ml}$ ) ( $n = 40$  beads from 3 mice for pneumolysin and control [without pneumolysin] groups, Mann–Whitney test). (I) Increased ciliary beating frequency in lateral ventricles of *Katnal2*-KO mice (P28–42), as measured by high-speed (approximately 1,000 frames/sec) time-lapse imaging and quantification of the beating frequency. Scale bar, 10  $\mu\text{m}$ . ( $n = 1,442$  ROIs from 67 cilia videos from 10 mice [WT-lateral], 1,346, 72, 9 [KO-lateral], Permutation test). (J) A working hypothesis suggesting that increased ependymal ciliary length and beating frequency would enhance CSF propulsion. The big arrow indicates the overall propulsion power of the cilia, and the small arrows indicate the forward directions of each ciliary movement. The additional cilium in the *Katnal2*-KO mice indicates increased beating frequency. (K) Increased CSF flow rates in the cerebral aqueduct of *Katnal2*-KO mice (P28–42), as measured by MRI. ( $n = 6$  mice [WT], 5 [KO], Student's *t* test). (L) Comparable ICPs in WT and *Katnal2*-KO mice (3 months). ( $n = 9$  mice [WT], 6 [KO], Student's *t* test). Data values represent means  $\pm$  SEM. Significance is indicated as \* ( $<0.05$ ), \*\* ( $<0.01$ ), \*\*\* ( $<0.001$ ), or ns (not significant). Statistical results and numerical data values can be found in [S1 Data](#). CSF, cerebrospinal fluid; ICP, intracranial pressure; KO, knockout; MRI, magnetic resonance imaging; WT, wild type.

<https://doi.org/10.1371/journal.pbio.3002596.g003>



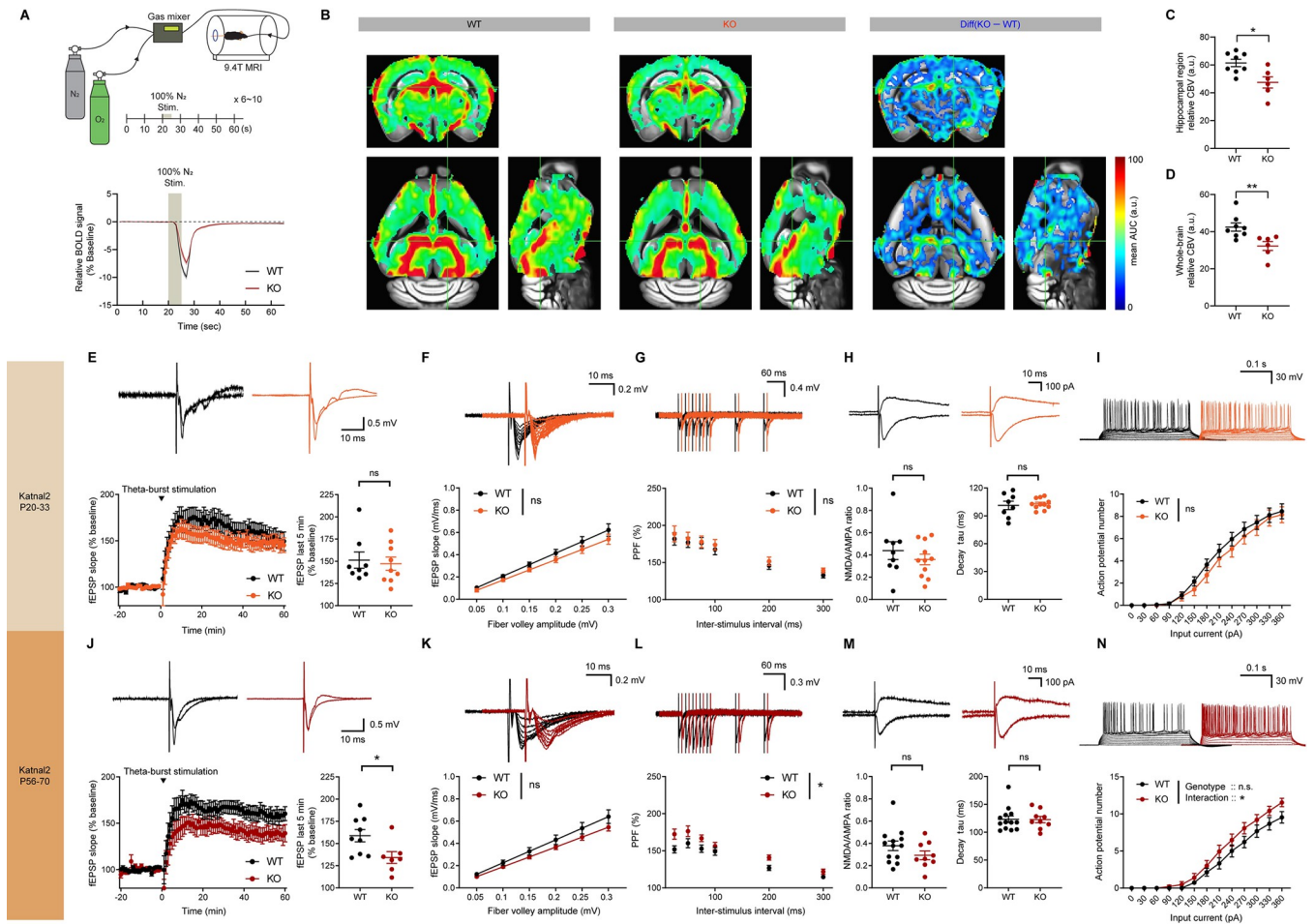


**Fig 4. Progressive synaptic deficits in the *Katnal2*-KO hippocampus.** (A–D) Decreased CBVs in various brain regions of *Katnal2*-KO mice, including the hippocampus surrounded by lateral ventricles, as compared with WT mice (3 months). CBV-weighted MRI measurements were performed with nitrogen stimuli in WT and *Katnal2*-KO mouse brains, and the relative CBV index was computed by the integration of the area under the curve (A). Note that the color-coded decreases in CBVs in *Katnal2*-KO mice occur in various brain regions (B, left and middle), although it seems to be greater in the mutant hippocampus (B, right). The results of the quantification of relative CBV indices are shown in (C) and (D) for the hippocampus and whole brain and in **S7A Fig** for various cortical and subcortical regions. ( $n = 8$  mice [WT], 6 [KO], Student’s *t* test). (E) Normal TBS-LTP at *Katnal2*-KO hippocampal SC-CA1 synapses (P26–33; last 5 min). ( $n = 7$  slices from 3 mice [WT], 9, 3 [KO], Student’s *t* test [last 5 min]). (F) Normal basal transmission at *Katnal2*-KO SC-CA1 synapses (P25–30), as measured by input-output curves. ( $n = 7, 3$  [WT], 8, 4 [KO], two-way RM-ANOVA). (G) Normal paired pulse facilitation at *Katnal2*-KO SC-CA1 synapses (P25–30). ( $n = 9, 4$  [WT], 10, 4 [KO], two-way RM-ANOVA). (H) Normal ratios of NMDA- and AMPAR-mediated EPSCs (NMDA/AMPA ratios) at *Katnal2*-KO SC-CA1 synapses (P20–21). ( $n = 9$  neurons from 4 mice [WT], 11, 4 [KO], Student’s *t* test). (I) Normal neuronal excitability in *Katnal2*-KO CA1 pyramidal neurons (P26–30), as measured by input-firing curves. ( $n = 20, 3$  [WT], 14, 3 [KO], two-way RM-ANOVA). (J) Suppressed TBS-LTP at *Katnal2*-KO SC-CA1 synapses (P56–70). ( $n = 9, 4$  [WT], 7, 3 [KO], Student’s *t* test). (K) Normal input-output ratio at *Katnal2*-KO SC-CA1 synapses (P56–70). ( $n = 9, 3$  [WT], 9, 4 [KO], two-way RM-ANOVA). (L) Suppressed paired pulse facilitation at *Katnal2*-KO SC-CA1 synapses (P56–70). ( $n = 10, 4$  [WT], 10, 4 [KO], two-way RM-ANOVA with Sidak’s test). (M) Normal NMDA/AMPA ratios at *Katnal2*-KO SC-CA1 synapses (P56–70). ( $n = 13, 5$  [WT], 9, 5 [KO], Mann–Whitney test [NMDA/AMPA ratio], Student’s *t* test [decay tau]). (N) Moderately increased excitability of *Katnal2*-KO CA1 pyramidal neurons (P56–70). ( $n = 15, 4$  [WT], 15, 4 [KO], two-way RM-ANOVA with Sidak’s test). Data values represent means  $\pm$  SEM. Significance is indicated as \* ( $<0.05$ ), \*\* ( $<0.01$ ), \*\*\* ( $<0.001$ ), or ns (not significant). Statistical results and numerical data values can be found in **S1 Data**. CBV, cerebral blood volume; EPSC, excitatory postsynaptic current; KO, knockout; MRI, magnetic resonance imaging; WT, wild type.

<https://doi.org/10.1371/journal.pbio.3002596.g004>

At adult stages (P56–70), TBS-LTP was suppressed at *Katnal2*-KO SC-CA1 synapses; there was no change in basal synaptic transmission or the NMDA/AMPA ratio, although presynaptic release and neuronal excitability were moderately increased (**Fig 4J–4N**). This suggests that the decrease in TBS-LTP at adult *Katnal2*-KO synapses does not involve a decrease in NMDAR function. These results collectively suggest that *Katnal2* KO in mice suppresses synaptic functions in the adult but not juvenile hippocampus.

## Progressive synaptic and ASD-related transcriptomic changes in *Katnal2*-KO mice

To gain insights into the mechanisms underlying the behavioral, ciliary, and synaptic deficits observed in *Katnal2*-KO mice in an unbiased manner, we analyzed transcriptomic changes in *Katnal2*-KO brains at P21 and P70 by RNA-Seq analyses.

The RNA-Seq analyses revealed that there were small sets of differentially expressed genes (DEGs;  $p < 0.05$  and fold-change  $> 1.5$ ) at both P21 and P70, as shown by volcano plots (28 up- and 11 down-regulated at P21, and 81 up- and 66 down-regulated at P70) (S8 Fig and S2 Data and S3 Data). DAVID analyses of these DEGs yielded no significant gene ontology (GO) terms, likely because there were relatively few DEGs.

We next attempted a gene set enrichment analysis (GSEA), which uses the whole list of ranked transcripts (i.e., by  $p$  values) rather than a small fraction of transcripts above arbitrary cutoffs. This enables an unbiased exploration of altered biological functions [48]. Our results identified distinct biological functions as being altered in the *Katnal2*-KO transcriptomes at P21 and P70 (termed P21-*Katnal2*/WT and P70-*Katnal2*/WT transcripts, respectively). Specifically, P21-*Katnal2*/WT transcripts were positively, although moderately, enriched for vacuole- and extracellular matrix-related gene sets (meaning these genes were up-regulated), and negatively and moderately enriched for splicing- and cell morphogenesis-related gene sets in the cellular component (CC), biological process (BP), and molecular function (MF) domains, as shown by clusters of enriched gene sets generated using Cytoscape EnrichmentMap App [49] (Fig 5A and S4 Data).

At P70, *Katnal2*/WT transcripts were positively and strongly enriched for ribosome/mitochondria-related gene sets, and negatively and strongly enriched for synapse-related gene sets in the C5-CC, C5-BP, and C5-MF domains, as shown by top-five gene set lists and EnrichmentMap gene-set clusters [49] (Fig 5B and S4 Data). These results suggest that P21-*Katnal2*/WT and P70-*Katnal2*/WT transcripts are associated with distinct biological functions and that P70-*Katnal2*/WT transcripts display more strongly up-regulated ribosome/mitochondria-related genes and down-regulated synapse-related genes, as compared with P21-*Katnal2*/WT transcripts.

To determine if these transcriptomic changes are associated with ASD-related gene expression patterns, we performed GSEA using gene sets that are up- or down-regulated in ASD [50–54]. The results revealed that P21-*Katnal2*/WT transcripts were positively enriched for ASD-related gene sets that are up-regulated in ASD (DEG\_Up and Co-Exp\_Up), but not significantly enriched for those down-regulated in ASD (DEG\_Down and Co-Exp\_Down) (Fig 5C and S5 Data). In addition, P21-*Katnal2*/WT transcripts were negatively enriched for 2 of the 6 ASD-risk gene sets that are usually down-regulated in ASD (SFARI [all] and ASD\_AutismKB, but not FMRP target, DeNovoMiss or DeNovoVariants) (Fig 5C). These results indicate that P21-*Katnal2*/WT transcripts are moderately enriched for ASD-related/risk gene sets (partial “ASD-like” pattern).

P70-*Katnal2*/WT transcripts showed a much stronger ASD-like pattern: They were positively enriched for Co-Exp\_Up, negatively enriched for Co-Exp\_Down, and negatively enriched for 5 out of the 6 ASD-risk gene sets (SFARI [all and high-confidence], FMRP target, DeNovoMiss, and DeNovoVariants, but not ASD\_AutismKB) (Fig 5C). These results suggest that there are stronger ASD-like transcriptomic patterns in P70 *Katnal2*-KO mice relative to P21 *Katnal2*-KO mice.

When GSEA was performed against cell type-specific gene sets that are distinctly enriched in ASD [50–55], P21-*Katnal2*/WT transcripts were largely negatively enriched for neuron (both glutamate and GABA)-related gene sets and positively enriched for glia (astrocyte and

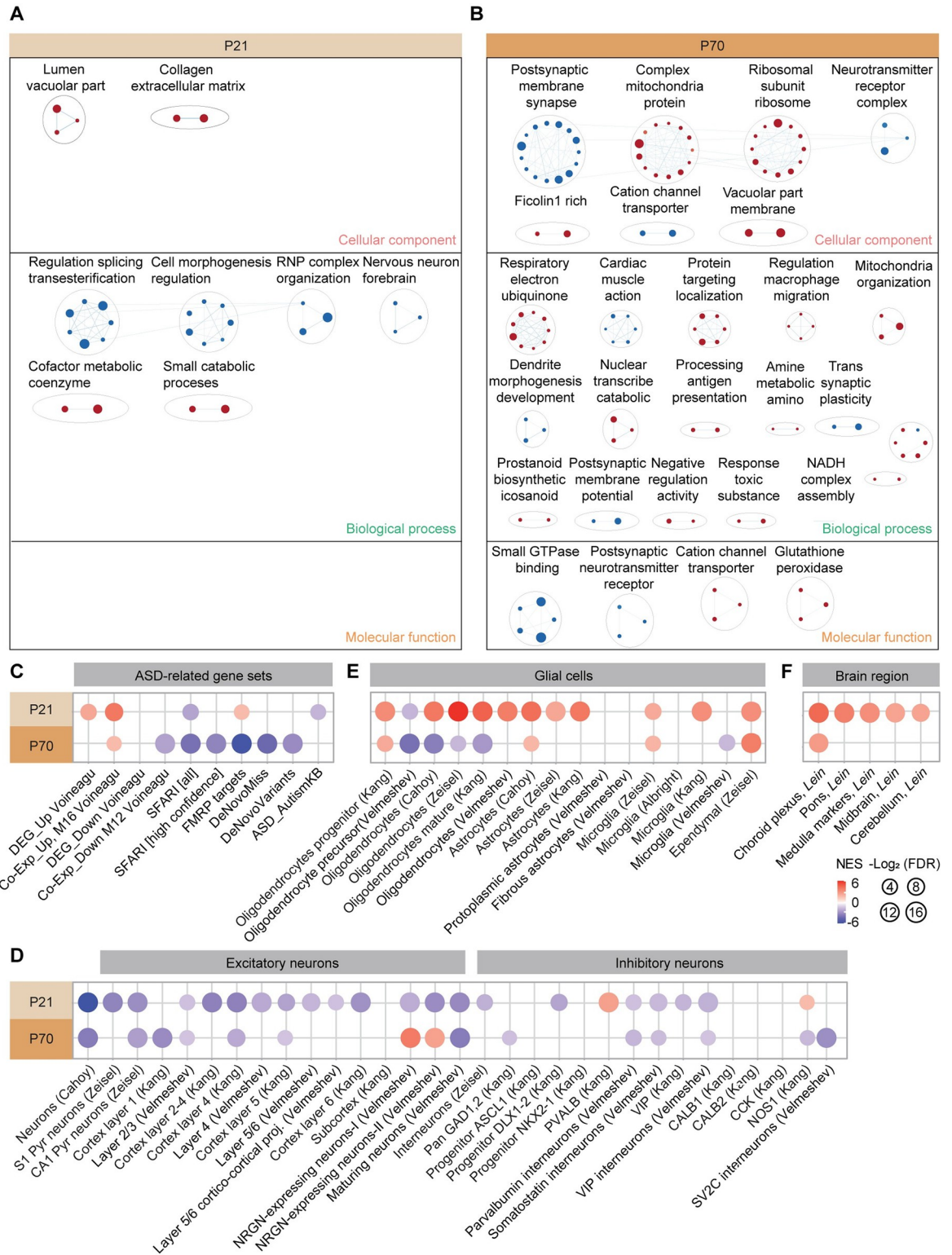


**Fig 5. Progressive synaptic and ASD-related transcriptomic changes in *Katnal2*-KO mice.** (A and B) GSEA results revealing the enrichment of P21- and P70-*Katnal2*/WT transcripts (whole brains) for biological functions, as shown by the list of top-five positively (red) and negatively (blue) enriched gene sets in the CC domain (left) and the clusters of enriched gene sets visualized using EnrichmentMap Cytoscape App (right). (C) GSEA results assessing *Katnal2*/WT transcripts for ASD-related gene sets that are up-regulated in ASD (DEG\_Up and Co-Exp\_Up), down-regulated in ASD (DEG\_Down and Co-Exp\_Down), and ASD-risk gene sets that

are usually down-regulated in ASD (SFARI [all], SFARI [high-confidence], FMRP target, DeNovoMiss, and DeNovoVariants, but not ASD\_AutismKB). ( $n = 5$  mice for WT and KO, FDR < 0.05). (D) GSEA results assessing *Katnal2*/WT transcripts for neuron type-specific gene sets (excitatory and inhibitory neuronal) that are usually down-regulated in ASD. ( $n = 5$  mice for WT and KO, FDR < 0.05). (E) GSEA results assessing *Katnal2*/WT transcripts for glial cell type-specific gene sets that are usually down-regulated in oligodendrocytes and up-regulated in astrocytes and microglia in ASD. ( $n = 5$  mice for WT and KO, FDR < 0.05). (F) GSEA results assessing *Katnal2*/WT transcripts for brain region-related gene sets. ( $n = 5$  mice for WT and KO, FDR < 0.05). Raw RNA-Seq data and detailed GSEA results can be found in [S2 Data](#) and [S4 Data](#). ASD, autism spectrum disorder; CC, cellular component; DEG, differentially expressed gene; FDR, false discovery rate; GSEA, gene set enrichment analysis; KO, knockout; WT, wild type.

<https://doi.org/10.1371/journal.pbio.3002596.g005>

microglia)-related gene sets; the directions were mainly in line with the those observed in ASD (ASD-like), although oligodendrocyte-related gene sets were positively enriched (“reverse-ASD” direction) ([Fig 5D and 5E](#)). Notably, P70-*Katnal2*/WT transcripts showed largely similar but weakened negative enrichments for neuron-related gene sets and positive enrichments for glia (including oligodendrocyte)-related gene sets ([Fig 5D and 5E](#)). Intriguingly, both P21 and P70 *Katnal2*/WT transcripts were positively enriched for an ependymal cell-related gene set ([Fig 5E](#)) and for a choroid plexus-related gene set ([Fig 5F](#)), which is in line with the strong expression of *Katnal2* in ventricular structures ([Fig 2A](#)).

Therefore, the P21 and P70 transcriptomes in *Katnal2*-KO mice seem to display the following age-dependent and progressive changes: (1) weak changes in biological functions at P21, but strong biological changes at P70 (i.e., synaptic down-regulation); (2) stronger ASD-like expressional changes in ASD-related/risk gene sets at P70 compared with P21; (3) stronger ASD-like changes in neuronal and glial (astrocyte/microglia) gene expressions at P21 relative to P70, with the exception of oligodendrocytes (being more ASD-like at P70); and (4) ependymal and choroid plexus-related gene up-regulations at both P21 and P70.

### **Katnal2 gene re-expression prevents ependymal ciliary, ventricular, and behavioral phenotypes**

We hypothesized that if *Katnal2* KO leads to the ventricular enlargements and behavioral deficits observed in *Katnal2*-KO mice, *Katnal2* gene re-expression may rescue these deficits if attempted as early as possible. To assess this possibility, we employed AAV (PHP.eB)-mediated *Katnal2* gene re-expression in the mutant mouse brain using early postnatal (P8–12) intracerebroventricular injection, at a time point when the ventricular enlargements were not yet evident. We then performed brain/ciliary morphological and behavioral analysis in adult mice (P56–70) ([Fig 6A](#)).

Early postnatal *Katnal2* re-expression with stronger gene expression in ventricular regions ([Fig 6B](#)) restored ependymal ciliary length and ventricular enlargement in adult *Katnal2*-KO mice, as compared with controls (*Katnal2*-KO mice without *Katnal2* re-expression and WT mice with EGFP/control overexpression) ([Fig 6C and 6D](#)). Early *Katnal2* re-expression also partially prevented the abnormal increase in courtship USVs in adult *Katnal2*-KO mice, as supported by the comparable USV levels in *Katnal2*-re-expressing *Katnal2*-KO mice and WT mice with EGFP overexpression, although USV levels in *Katnal2*-KO mice with re-expression did not significantly differ from those in *Katnal2*-KO mice without re-expression ([Fig 6E](#)).

These results suggest that early postnatal *Katnal2* re-expression in *Katnal2*-KO mice prevents ependymal ciliary lengthening, ventricular enlargements, and courtship USV deficits in adult mutant mice.

### **Discussion**

In the present study, we found that *Katnal2* KO in mice leads to autistic-like abnormal social communications. These changes accompanied age-dependent progressive ventricular

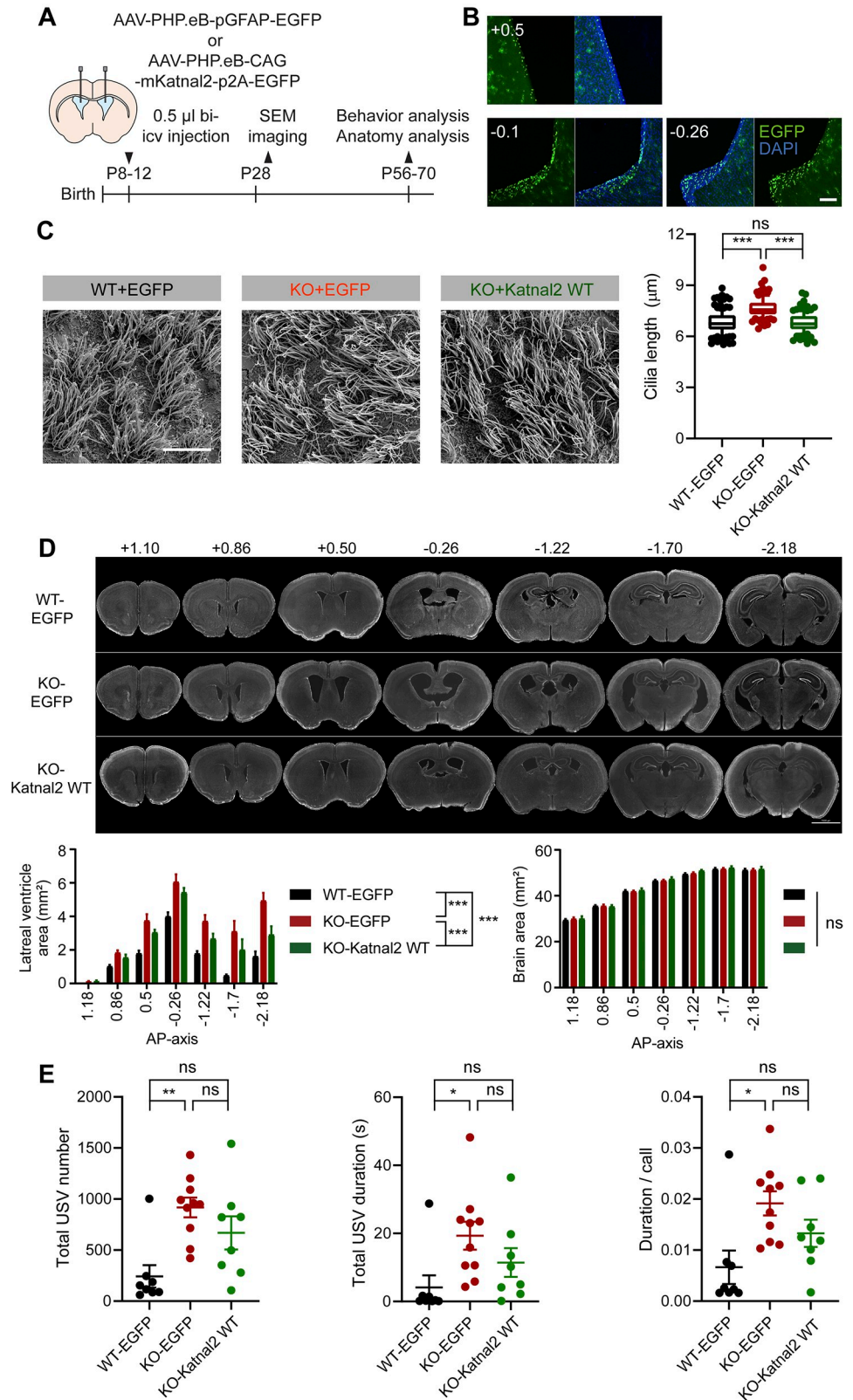


**Fig 6. Early *Katnal2* gene re-expression prevents ciliary, ventricular, and behavioral phenotypes in adult *Katnal2*-KO mice.** (A) Schematic diagram of *Katnal2* re-expression experiments in which PHP.eB.AAV-

pCAG-Katnal2-p2A-EGFP, or control virus (PHP.eB.AAV-pGFAP-EGFP; pGFAP for ependymal cell expression), was bilaterally injected into the lateral ventricles (intracerebroventricular/icv injection) of WT or *Katnal2*-KO mice at approximately P8–12, and the effects on ventricles and behaviors were determined at adult stages (approximately P56–70). (B) Examples of *Katnal2* re-expression (marked by EGFP) in the lateral ventricles of *Katnal2*-KO brain (P56). The numbers above brain images indicate anterior-posterior positions. Scale bar, 200  $\mu$ m. (C) Prevention of ependymal ciliary lengthening in the *Katnal2*-KO brain (P28–32) by early postnatal *Katnal2* re-expression (P8–12), as compared with control conditions (*Katnal2*-KO-EGFP alone and WT-EGFP alone). ( $n = 160$  cilia from 16 images from 4 mice [WT-EGFP alone/control], 120, 12, 3 [KO-EGFP alone], and 120, 12, 3 [KO-rescue/*Katnal2* re-expression], one-way ANOVA with Sidak's test). Scale bar, 10  $\mu$ m. (D) Prevention of ventricular enlargement in the *Katnal2*-KO brain (P56–70) by early postnatal *Katnal2* re-expression (P8–12), as compared with control conditions (*Katnal2*-KO-EGFP alone and WT-EGFP alone). Note that the brain areas are minimally affected by the treatments. ( $n = 22$  mice [WT-EGFP alone/control], 8 [KO-rescue/*Katnal2* re-expression], and 20 [KO-EGFP alone], two-way RM-ANOVA with Sidak's test). Scale bar, 2 mm. (E) Partial prevention of excessive courtship USVs in *Katnal2*-KO mice (P56–70) by early postnatal *Katnal2* re-expression (P8–12), as compared with control conditions (*Katnal2*-KO-EGFP alone [not significant] and WT-EGFP alone [not significant, meaning rescued]). ( $n = 8$  [WT-EGFP alone], 10 [KO-EGFP alone], and 8 [KO-rescue], one-way ANOVA with Sidak's test). Data values represent means  $\pm$  SEM. Significance is indicated as \* ( $<0.05$ ), \*\* ( $<0.01$ ), \*\*\* ( $<0.001$ ), or ns (not significant). Statistical results and numerical data values can be found in [S1 Data](#). KO, knockout; USV, ultrasonic vocalization; WT, wild type.

<https://doi.org/10.1371/journal.pbio.3002596.g006>

enlargements involving lengthened ependymal cilia and increased ciliary beating frequency. Similar progressive impairments were observed in synaptic functions and transcriptomic patterns. In addition, early postnatal *Katnal2* re-expression prevented ependymal ciliary, ventricular, and behavioral deficits in mutant adults, causally linking *Katnal2* KO with the phenotypes.

*Katnal2*-KO mice show social deficits, including abnormally increased USVs during courtship and reduced success of mounting after the initial social interactions in male mice, and avoidance of a second social interaction with a mutant male after the initial interaction in female mice. Because USV levels are correlated with social interaction levels in rodents [56], the excessive USVs in *Katnal2*-KO males in the face of decreased mounting success, which would substantially decrease reproductive success, may represent increased effort of male mutant mice for additional social interactions.

An important *Katnal2*-KO phenotype is age-dependent and progressive ventricular enlargement (ventriculomegaly), as shown by slice-staining and MRI results. The increased flow rate of CSF in the mutant cerebral aqueduct, measured by MRI, may reflect increased pressure of the CSF in the upstream lateral and third ventricles. However, the intracranial pressure was comparable in WT and *Katnal2*-KO mice, suggesting that an increase in CSF pressure might have been relieved by an increase in ventricular volume. Indeed, normal pressure is common in hydrocephalus, including the idiopathic normal-pressure hydrocephalus, which involves dilated ventricles, cognitive deficit, and neural symptoms [57–59]. Notably, the ventricular enlargement in the *Katnal2*-KO brain did not increase the total brain volume, likely because of the progressive nature of the ventriculomegaly. However, prominent macrocephaly and abnormal head shapes were observed in approximately 10% of *Katnal2*-KO mice, and these mice failed to survive beyond approximately P40. This suggests that *Katnal2* KO leads to strong macrocephaly in some penetrant cases.

Ventricular enlargements in *Katnal2*-KO mice could be caused by impaired formation or function of ependymal cilia, considering that *Katnal2* is highly expressed in ependymal cells and the choroid plexus in the mouse brain. Indeed, many of previous studies have reported impaired formation and function of ependymal cilia as the cause of hydrocephalus [60]. However, our data indicate that *Katnal2* KO induces lengthened ependymal ciliary and enhanced ependymal ciliary function (increases in ciliary bead flow and beating frequency). These results suggest that *Katnal2* negatively regulates ependymal ciliary length. Moreover, the lengthened ependymal cilia with increased beating frequency may strongly propel CSF down the stream and cause ventriculomegaly by exerting increased hydraulic stress on periventricular tissues,

although the measured intracranial pressure was normal, again suggestive of a pressure release by increased ventricular volume. This proposed mechanism of ventriculomegaly differs radically from the previously reported mechanisms for hydrocephalus, such as impaired formation and function of ependymal cilia.

An important question would be whether the ventriculomegaly in *Katnal2*-KO mice has any functional influence on nearby brain regions, such as the hippocampus, which is surrounded by the enlarged lateral ventricles. Our MRI data indicate that the blood volumes in various mutant brain regions, including the hippocampus, are decreased. This could limit the supply of nutrients and oxygen to neurons and glial cells, which would further aggravate local blood volume and flow [61]. In line with these changes, presynaptic release and postsynaptic synaptic plasticity are progressively suppressed in the *Katnal2*-KO hippocampus. This coincides with the progressive ventriculomegaly in *Katnal2*-KO mice as well as the observed progressive transcriptomic changes, including synaptic gene down-regulations and ASD-like transcriptomes. These results constitute strong temporal correlations across the molecular/transcriptomic, synaptic, and ventricular phenotypes in *Katnal2*-KO mice.

Another key question would be whether *Katnal2* KO is causally associated with the *Katnal2*-KO phenotypes. In support of this, early postnatal *Katnal2* re-expression driven by intracerebroventricular virus injection prevents the ependymal ciliary enlengthening and ventricular enlargements and partially prevents the courtship USV deficits from occurring in adult *Katnal2*-KO mice. These results suggest there could be therapeutic potential in normalizing *Katnal2* expression at early postnatal stages. This is in line with the emerging evidence indicating the importance of early corrections in animal models of ASD [62].

A previous study on mice lacking *Katnal1*, which is a *Katnal2*-related MT-severing protein [63], reported ventricular enlargement, morphological and functional ciliary deficits, and pup USV communication deficits [64]. *KATNAL1* mutations in humans have been associated with intellectual disability and microcephaly [65] but minimally with ASD (only 1 ASD-related mutation has been reported thus far) [66]. This contrasts with the large number of ASD-risk *KATNAL2* mutations reported to date (49 genetic variants) [22–29]. Therefore, our results extend the notion that MT-related dysfunction can be linked to ependymal/ciliary/ventricle/CSF deficits in ASD, in addition to their impacts on intellectual disability and microcephaly. Our study also suggests that ependymal ciliopathies could underlie ASD, providing new mechanistic insights that expand the previously reported bases for ASD pathophysiology (i.e., synapses, signaling, chromatin, and transcription) [67–70].

Lastly, while revising the manuscript, there was a preprint publication of a similar study on *Katnal2*-KO mice that display ventriculomegaly [71]. This mutant line lacks exon 8 and is “qualitatively” different from our *Katnal2* mouse line that lacks exon 3. Their exon 8 deletion leads to an in-frame deletion in a segment (aa 220–245; 26 aa residues) immediately preceding the AAA-ATPase domain located in the middle of the *Katnal2* protein [539 aa-long], likely leaving the exon 8-lacking *Katnal2* protein variant largely similar to the whole protein although it might destabilize the protein, which was not directly tested. On the other hand, our exon 3 deletion leads to an out-of-frame protein-truncating mutation in the N-terminal region of the *Katnal2* protein at around approximately aa 69, almost completely eliminating the whole *Katnal2* protein. The abovementioned preprint publication also reports another *Katnal2* mouse line lacking exons 2–12, a larger deletion compared with the exon 8 deletion. However, this mouse line was used to measure ventriculomegaly and choroid plexus-related measures but not other phenotypes that help infer how the ventriculomegaly was induced such as ependymal ciliary functions, making it unclear if the ventriculomegaly observed in these mice involves decreased or increased ependymal ciliary function. These differences and uncertainties should be clarified in future studies.

In summary, our results indicate that deletion of *Katnal2*, which is highly expressed in ependymal cells, leads to ASD-like social communication deficits that are associated with ventricular enlargements, enhanced ependymal ciliary function, suppressed synaptic function, and ASD-like transcriptomic changes.

## Materials and methods

### Animals

ES cells containing the *Katnal2*-targeted allele were received from EUCOMM (MAE-4330; *Katnal2*<sup>tm1a(EUCOMM)Wtsi</sup>) and used to generate transgenic mice. The first-generation mice were backcrossed with mice of C57BL/6J background for more than 5 generations before experiments were conducted. Mating with Protamine-Flp mice was used to generate *Katnal2*<sup>fl/+</sup> mice. Fertilized eggs (from the breeding with C57BL/6J WT mice) at the two-cell embryo stage were treated with purified HTNC, a cell-permeable Cre recombinase, at a final concentration of 0.3  $\mu$ M for 30 to 40 min. *Katnal2*-KO mice were genotyped by polymerase chain reaction (PCR) using the following primer sets: *Katnal2* allele: Fwd = 5'-AACAGTGGGAA-CATCACCAGA-3'; Rev = 5'-TCAAACAACCCAGGCACTCA-3'. The expected size of KO PCR band is 259 bp, while WT band is 215 bp. Thy1-EGFP mice were from Jackson Laboratory (Tg(Thy1-EGFP)Mjrs/J). All mice were housed and bred at the mouse facility of Korea Advanced Institute of Science and Technology (KAIST) and maintained according to the Animal Research Requirements of KAIST. All animals were fed ad libitum and housed under 12 h light/dark cycle (light phase from 1 AM to 1 PM). Mice were weaned at around the age of post-natal day 21, and mixed-genotype littermate mice of the same sex were housed together until experiments. All animal procedures were approved by the Committee of Animal Research at KAIST (KAIST; KA2020-80) that are adhering to the Animal Protection Act and the Laboratory Animal Act of the Korean government.

### Immunohistochemistry

Mouse brain slices (50  $\mu$ m; vibratome, Leica) were prepared and stained with DAPI-containing Vectashield (Vector Laboratory) and for Cux1 and FoxP2 using the following commercial antibodies: Cux1 (Santa Cruz sc-13024 at 1:500) and FoxP2 (Abcam ab16046 at 1:500).

### X-gal staining

X-gal staining for *Katnal2*- $\beta$ -galactosidase fusion proteins was performed using brain slices (100- $\mu$ m coronal sections) from *Katnal2*-KO cassette-containing mice (MAE-4330; *Katnal2*<sup>tm1a(EUCOMM)Wtsi</sup>; P21 and P56) and X-gal staining (20 mg/ml X-gal; in 2 mM MgCl<sub>2</sub>, 5 mM K<sub>4</sub>Fe(CN)<sub>6</sub>·3H<sub>2</sub>O (Sigma #P-8131), 5 mM K<sub>3</sub>Fe(CN)<sub>6</sub>, 0.01% DOC, 0.02% NP-40 in 1 $\times$  PBS).

### Combining fluorescence in situ hybridization with immunohistochemistry

Frozen sections (14- $\mu$ m thick) were cut coronally through the third or fourth cerebral ventricle. Sections were thaw-mounted onto Superfrost Plus Microscope Slides (Fisher Scientific 12-550-15). The sections were fixed in 4% paraformaldehyde (PFA) for 10 min, dehydrated in increasing concentrations of ethanol for 5 min, and finally air-dried. Tissues were then pre-treated for protease digestion for 10 min at room temperature. For RNA detection, incubations with different amplifier solutions were performed in a HybEZ hybridization oven (ACDBio) at 40°C. The probe used in this study was 3 synthetic oligonucleotides complementary to the nucleotide (nt) sequence 170–1177 of Mm-*Katnal2* (ACDBio). The labeled probe was conjugated to Atto 550 (C1). The sections were hybridized at 40°C with labeled probe per slide for 2



h. Then, the nonspecifically hybridized probe was removed by washing the sections, 3 times each in 1× wash buffer at room temperature for 2 min. Amplification steps involved sequential incubations at 40°C with Amplifier 1-FL for 30 min, Amplifier 2-FL for 15 min, Amplifier 3-FL for 30 min, and Amplifier 4 Alt B-FL for 15 min. Each amplifier solution was removed by washing 3 times with 1× wash buffer for 2 min at RT. Then, sections were postfixed in 4% PFA for 1 h at room temperature and washed with phosphate-buffered saline (PBS). Next, the sections were incubated in primary antibody for 1 h at 37°C. The primary antibodies were diluted in PBS containing 3% BSA and 0.2% Triton X-100. The following primary antibodies were used: acetylated tubulin (Sigma #T6793, 1:500), FoxJ1 (human/mouse, eBioscience #14-9965-82, 1:500), and S100 (Dako #Z0311, 1:500). Next, the sections were washed with PBS and incubated in a cocktail of 488 or 647 conjugated secondary antibodies (Jackson #711-096-152, #715-605-152, and Invitrogen #21202 [1:500]) in PBS containing 3% BSA and 0.2% Triton X-100 for 1 h at room temperature. The secondary antibody was washed with PBS and further incubated with Hoechst (Invitrogen #H3570, 1:1,000) at RT for 10 min. The sections were immersed in mounting solution and images were captured using a confocal microscope (TCS SP8, Leica).

### RNA-Seq analysis

Five mice of 3 and 10 weeks of age were used for each group (WT and KO). The extracted mouse brains were preserved in RNAlater solution (Ambion) and stored at -80°C. Poly-T oligo-attached magnetic beads were utilized to purify poly-A mRNAs. RNA concentrations were quantified using Quant-IT RiboGreen (Invitrogen, R11490), and RNA integrity was determined using TapeStation RNA screen tape (Agilent Technologies), after which only high-quality RNAs (RIN > 7.0) were selected for cDNA library construction using Illumina TruSeq mRNA Sample Prep kit v2 (Illumina). Indexed libraries were submitted to an Illumina HiSeq 4000 (Illumina), and paired-end (2 × 100 bp) sequencing was performed by Macrogen. Transcript abundance was estimated with Salmon (v1.1.0) [72] in Quasi-mapping-based mode onto the *Mus musculus* genome (GRCm38) with GC bias correction (-gcBias). The acquired abundance data was imported to R (v.3.5.3) with tximport [73] package and differential gene expression analysis was performed using R/Bioconductor DEseq2 (v1.30.1) [74]. Normalized read counts were computed by dividing the raw read counts by size factors and fitted to a negative binomial distribution. The *p* values were adjusted for multiple testing with the Benjamini-Hochberg correction. Genes with an adjusted *p* value of less than 0.05 were considered as differentially expressed. GSEA [75,76] was performed to determine whether a priori-defined gene sets would show statistically significant differences in expression between WT and *Katnal2*-mutant mice. Enrichment analysis was performed using GSEAPreranked (gsea-3.0.jar) module on gene set collections downloaded from Molecular Signature Database (MSigDB) v7.0. GSEAPreranked was applied using the list of all genes expressed, ranked by the fold change, and multiplied by the inverse of the *p* value with recommended default settings (1,000 permutations and a classic scoring scheme). The false discovery rate (FDR) was estimated to control the false positive finding of a given normalized enrichment score (NES) by comparing the tails of the observed and null distributions derived from 1,000 gene set permutations. The gene sets with an FDR of less than 0.05 were considered as significantly enriched. Integration and visualization of the GSEA results were performed using the EnrichmentMap Cytoscape App (version 3.8.1) [49,77].

### Electrophysiology

Sagittal mouse hippocampal slices (400 and 300 μm thickness for extracellular and intracellular recordings, respectively) were prepared using a vibratome (Leica VT1200) in ice-cold

dissection buffer containing (in mM) 212 sucrose, 25 NaHCO<sub>3</sub>, 5 KCl, 1.25 NaH<sub>2</sub>PO<sub>4</sub>, 0.5 CaCl<sub>2</sub>, 3.5 MgSO<sub>4</sub>, 10 D-glucose, 1.25 L-ascorbic acid, and 2 Na-pyruvate bubbled with 95% O<sub>2</sub>/5% CO<sub>2</sub>. The slices were recovered at 32°C for 1 h in normal ACSF (in mM: 125 NaCl, 2.5 KCl, 1.25 NaH<sub>2</sub>PO<sub>4</sub>, 25 NaHCO<sub>3</sub>, 10 glucose, 2.5 CaCl<sub>2</sub>, and 1.3 MgCl<sub>2</sub> oxygenated with 95% O<sub>2</sub>/5% CO<sub>2</sub>). For the recording, a single slice was moved to and maintained in a submerged-type chamber at 28°C, continuously perfused with ACSF (2 ml/min) saturated with 95% O<sub>2</sub> and 5% CO<sub>2</sub>. Stimulation and recording pipettes were pulled from borosilicate glass capillaries (Harvard Apparatus) using a micropipette puller (Narishige).

For extracellular recordings, mouse hippocampal slices (P20–33/juvenile and P56–70/adult) were recorded in the CA1 stratum radiatum region using pipettes filled with ACSF (1 MΩ). fEPSPs were amplified (Multiclamp 700B, Molecular Devices) and digitized (Digidata 1440A, 1550, Molecular Devices) for measurements. The Schaffer collateral pathway was stimulated every 20 s with pipettes filled with ACSF (0.3 to 0.5 MΩ). The stimulation intensity was adjusted to yield a half-maximal response, and 3 successive responses were averaged and expressed relative to the normalized baseline. To induce LTP by theta-burst stimulation (40 trains [4 stimuli/train at 100 Hz with inter-train intervals of 170 ms] separated in 4 bursts [10 trains/burst with inter-burst intervals of 1 s]) after the acquisition of a stable baseline. For input/output recording, a series of increasing input stimuli were given to evoke output signals, after acquiring stable baseline. Fiber volleys and fEPSP slopes that are measured were interpolated by linear fits to plot input/output signal relationships. The paired-pulse ratio was measured across a range of inter-stimulus intervals of 25, 50, 75, 100, 200, and 300 ms.

Whole-cell patch-clamp recordings of hippocampal CA1 pyramidal neurons were made using a MultiClamp 700B amplifier (Molecular Devices) and Digidata 1440A, 1550 (Molecular Devices). During whole-cell patch-clamp recordings, the series resistance was monitored for each sweep by measuring the peak amplitude of the capacitance currents in response to short hyperpolarizing step pulse (5 mV, 40 ms); only cells with a change in <20% were included in the analysis. To measure NMDA/AMPA ratio, mouse hippocampal slices (P20–21/P56–70) were used. The recording pipettes (2.5 to 3.5 MΩ) were filled with an internal solution containing the following (in mM): 100 CsMeSO<sub>4</sub>, 10 TEA-Cl, 8 NaCl, 10 HEPES, 5 QX-314-Cl, 2 Mg-ATP, 0.3 Na-GTP and 10 EGTA, with pH 7.25, 295 mOsm. CA1 pyramidal neurons were voltage clamped at -70 mV, and EPSCs were evoked at every 15 s. AMPAR-mediated EPSCs were recorded at -70 mV, and 20 consecutive responses were recorded after stable baseline. After recording AMPAR-mediated EPSCs, holding potential was changed to +40 mV to record NMDAR-mediated EPSCs. NMDA component was measured at 60 ms after the stimulation. The NMDA/AMPA ratio was determined by dividing the mean value of 20 NMDA components of EPSCs by the mean value of 20 AMPAR-mediated EPSC peak amplitudes. Decaying tau of NMDA-R EPSC was measured since 60 ms after the stimulus to rule out intervening AMPA current. To measure excitability of hippocampal CA1 cells (P20–21/P56–70), recording pipettes (2.5 to 3.5 MΩ) were filled with an internal solution containing the following (in mM): 137 K-gluconate, 5 KCl, 10 HEPES, 0.2 EGTA, 10 Na-phosphocreatine, 4 Mg-ATP, and 0.5 Na-GTP, with pH 7.2, 280 mOsm. To inhibit postsynaptic responses, picrotoxin (100 μm), NBQX (10 μm), and D-AP5 (50 μm) were added. After rupturing the cell, the currents were clamped, and RMP was measured. Cells with RMP larger than -60 mV were not used. After stabilizing cell, RMP was adjusted by -65 mV. Current input was increased from 0 to 360 in increments of 30 pA per sweep. Each current was injected with a time interval of 15 s.

Data were acquired by Clampex 10.2 (Molecular Devices) and analyzed by Clampfit 10 (Molecular Devices). Drugs were purchased from Abcam (TTX), Tocris (NBQX, D-AP5), and Sigma (picrotoxin, DCS).

## Electron microscopy

For SEM, brain cortical tissues were harvested and fixed in 1% glutaraldehyde and 2% OsO<sub>4</sub> solution. After washing in 0.1 M sodium phosphate buffer (pH 7.2), samples were dehydrated using acetone in a sequential gradient and through the critical point dryer (Leica CPD300). After mounting, samples were coated with gold particles and observed on a field emission scanning electron microscope (Hitachi Regulus 8100). Adobe Photoshop was used for the analysis of ependymal ciliary length.

## Magnetic resonance imaging

All MRI experiments were performed on a Bruker Biospec 9.4 T/30 cm horizontal bore instrument with an actively shielded 12.0 cm diameter insert. Mice were initially anesthetized using 2% to 5% isoflurane. Then, the mouse was positioned in an MR cradle with a bite bar and ear bars, and maintained with 1.0% to 1.2% isoflurane at 37 ± 0.5°C using a circulating warm water blanket throughout MRI studies. A homogenous coil (86 mm inner diameter) was used for excitation, and an actively decoupled Bruker planar surface coil (10 mm inner diameter) positioned on top of the mouse head was used for detection.

For brain volume analysis, anatomical images were acquired using a T2 RARE sequence with a RARE factor of 4. Four averages of 20 axial slices were acquired with a field of view of 15 × 7.5 mm, a spatial resolution of 50 × 50 × 500 μm<sup>3</sup>, matrix size of 256 × 256, effective echo time (TE) of 30 ms, echo spacing of 15 ms, and recovery time (TR) of 4 s. The Allen mouse brain atlas (<https://atlas.brain-map.org/>) was spatially registered to individual anatomical images with Advanced Normalization Tools (ANTs) (<http://stnava.github.io/ANTs/>) [78]. The bilateral lateral ventricles were visually identified from anatomical images in each slice, and their volumes were determined. Also, regions of interest were identified, based on the Allen brain atlas, and their volumes were calculated from each 3D anatomical image in each animal.

For CSF flow analysis, 3D phase-contrast MRI with velocity encoding (FLOWMAP) was used for mapping CSF velocity. A velocity encoding coefficient of 4 cm/s was used in the slice direction. Sixteen averages of 20 axial slices were acquired with a resolution of 156 × 156 × 500 μm<sup>3</sup>, TE = 5 ms, TR = 17.461 ms, and flip angle = 20°. The flow images were analyzed with ParaVision 6.0.1 software (Bruker Biospin). The cerebral aqueduct appearing around in the midline brain regions was identified by visual inspections of anatomical images and flow maps as well as the brain atlas. Mean CSF velocity was determined in the 2 × 2 pixel ROI of the cerebral aqueduct.

For cerebral blood volume measurements [44], T<sub>2</sub><sup>\*</sup>-weighted single-shot GE-EPI were acquired with the following parameters: TR/ TE = 1,000/11.6 ms, flip angle = 50°, spatial resolution = 156 × 156 × 500 μm<sup>3</sup>, and 20 axial slices. Transient hypoxia was induced by reducing the fraction of inspired oxygen (FiO<sub>2</sub>) from approximately 50% to 0% with a three-channel programmable gas mixer (GSM-3 Gas Mixer, CWE) synchronized with the MRI scanner. A 150-s run consisted of 20-s normoxia, 5-s anoxia, 60-s normoxia, 5-s anoxia, and 60-s normoxia. Three to five runs were repeated and averaged. The Allen mouse brain atlas (<https://atlas.brain-map.org/>) was spatially registered to individual anatomical images with Advanced Normalization Tools (ANTs) (<http://stnava.github.io/ANTs/>) [78]. Thus, areas under the curve (AUC) over 20 s following the onset of 5-s stimulus were calculated at a voxel or ROI basis. The AUCs were normalized by an average across AUCs of vessel voxels (2 highest AUC voxels in each animal). Normalized AUCs are directly related to cerebral blood volume fraction (% blood volume).

## Beads flow assay

Ependymal flow analysis using fluorescent microbeads was performed as described [79]. Briefly, mice were sacrificed, and lateral walls (LWs) were exposed by removing the

hippocampus, cortex, thalamus, and choroid plexus in Leibovitz L-15 medium at 37°C. Then, the LWs were immobilized on a dissecting dish using 2 pins in fresh L-15 medium. A grinded glass microcapillary filled with FluoSpheres microbeads (2.0 μm diameter, Invitrogen, F8827) in 5% glycerol solution was positioned just above the dorsal-medial surface around the adhesion area of the LWs. Micro bead solution was carefully ejected using a Cell Tram Oil micro-manipulator (Eppendorf), and the movements of microbeads were recorded in 200 msec time intervals through ZEISS Axio Zoom.V16 fluorescent dissection microscope. High-speed videos of posterior-medial microbead flow were exported through ZEN Blue imaging software at 5.0 frames per second (fps). The speed of bead movement was measured using a manual tracking method in ImageJ program (fiji-win64). Pneumolysin (0.5 μg/ml) was treated in the L-15 media for 10 min prior to the experiment.

### Ciliary beating frequency

Coronal mouse lateral ventricle slices (250 μm thickness) were prepared using a vibratome (Leica VT1200) in ice-cold dissection buffer containing (in mM) 212 sucrose, 25 NaHCO<sub>3</sub>, 5 KCl, 1.25 NaH<sub>2</sub>PO<sub>4</sub>, 0.5 CaCl<sub>2</sub>, 3.5 MgSO<sub>4</sub>, 10 D-glucose, 1.25 L-ascorbic acid, and 2 Na-pyruvate bubbled with 95% O<sub>2</sub>/5% CO<sub>2</sub>. The slices were recovered at 32°C for 20 min in normal ACSF (in mM: 125 NaCl, 2.5 KCl, 1.25 NaH<sub>2</sub>PO<sub>4</sub>, 25 NaHCO<sub>3</sub>, 10 glucose, 2.5 CaCl<sub>2</sub>, and 1.3 MgCl<sub>2</sub> oxygenated with 95% O<sub>2</sub>/5% CO<sub>2</sub>). Prepared samples were imaged using Nikon Ti2 inverted microscope equipped with 60× objective lens (Nikon, Plan Apo 60× Oil). A microscope incubator (OKOLAB, H301-NIKON-TI-S-ER) was installed on the microscope to keep the sample at 37°C and 5% CO<sub>2</sub>. Live movies of beating cilia were acquired at the speed of approximately 1,000 fps using a high-speed camera (PCO, pco.dimax cs4).

To quantify ciliary beating frequency, 16~20 ROIs (11 × 11 pixels each; at least 30 pixels apart) were confined to the ependymal layers for each video. In each ROI, the brightness change was Fourier transformed to determine ciliary beating frequency. The custom MATLAB code used for the analysis is available in <https://github.com/sjleen/Cilia-stroke-analysis>.

### Intracranial pressure measurement

To measure intracranial pressure (ICP), mice were anesthetized with ketamine/xylazine and placed in a stereotaxic frame. The cisterna magna was exposed surgically, and a pressure transducer (FISO 75–0706) in an ACSF-filled glass-pulled capillary tube was positioned outside the membrane of the cisterna magna. A reference measurement was taken externally within the applied ACSF, and then the sensor was advanced into the cisterna magna. Pressure was recorded for a further 60 s using FISO Evolution software (v2.2.0.0). Traces were evaluated for patency, stability, and the presence of cardiorespiratory ICP waveforms and processed in R to calculate mean ICP during the measurement period.

### Katnal2 re-expression

To generate the *Katnal2*-overexpressing AAV construct (AAV-CAG-m*Katnal2*-p2A-EGFP-WPRE; WPRE for translational increase), the Myc-DDK/Flag-tagged mouse *Katnal2* cDNA (Origene #MR220406L1) construct was used to subclone mouse *Katnal2* cDNA into the AAV-CAG-GFP (Addgene #28014) vector. Here, some C-terminal aa sequence (aa 406–539) missing in the Origene mouse *Katnal2* clone and the p2A sequence (GSGATNFSLLKQAGDVEENPGP) were synthesized using overhang-PCR. AAV particles were prepared using HEK293T cells transfected with the target plasmid clone (abovementioned), PHP.eB plasmid (a kind gift from Dr. Viviana Gradinaru), and pAAV-helper. For virus injection into the lateral ventricles of the mouse brain, the head of mice (P8–12) were

fixed on stereotaxic apparatus (Kopf Instruments) under isoflurane (Piramal Healthcare) anesthesia. An injection needle containing virus solutions was moved down at the speed of 1 mm/min, and the solution was injected into the brain at the speed of 160 nL/min, 500 nL in total. Targets locations of the left and right ventricles (for bilateral injections) was DV (-2.0 mm), ML (-0.8/+1.0), and AP (+3.4) from the lambda on the skull (lambda was used instead of bregma because of the young age of the mouse). Their bregma-lambda length at P8–12 was 3.6 mm, shorter than that in adult mice (4.2 mm). As a negative control for AAV-CAG-mKatnal2-EGFP-WPRE, AAV-GFAP-EGFP was bilaterally injected. Both *Katnal2*-overexpressing AAV construct and control virus were bilaterally injected 0.5  $\mu$ l each.

### Immunoblot

Expression levels of *Katnal2* proteins were determined by immunoblot analyses. Because *Katnal2* protein levels in the brain were below the detection limit of immunoblotting using the currently available homemade *Katnal2* antibodies (#2167; guinea pig polyclonal), which targeted the last 30 aa (aa 517–539) of the mouse *Katnal2* protein, we used testis samples (8 weeks) prepared by tissue homogenization (150 mM NaCl, 1 mM EDTA, 50 mM Tris-HCl [pH = 7.4], 1% Triton-X100) and centrifugation followed by the use of the supernatant (not pellet).

For immunoblot analyses of choroid plexus lysates, 4 choroid plexus samples from 2 mice were pooled to make *n* of 1 and homogenized in RIPA buffer (10 mM HEPES, 150 mM NaCl, 1 mM EDTA, 0.1 mM MgCl<sub>2</sub>, 1% NP-40 with protease inhibitor). The following antibodies were utilized for immunoblotting: aquaporin-1 (Sigma-Aldrich, AB2219; 1:1,000), Na<sup>+</sup>/K<sup>+</sup>-ATPase  $\alpha$ 1 (Sigma-Aldrich, 05–369; 1:1,000), AE2 (Santa Cruz; sc-376632; 1:1,000), and GAPDH (Cell Signaling, D4C6R; 1:1,000). Full-length immunoblot images can be found in [S1 Raw Images](#).

### Behavioral experiments

Male mice were used for the behavioral experiments.

### Ultrasonic vocalization

An ultrasound microphone (Avisoft) and Avisoft Recorder software were used to record mouse USVs, a form of social communication in rodents [80]. For courtship USVs, a subject male mouse was placed in a new home cage with an age-matched unfamiliar C57BL/6J female mouse, followed by USV recordings for 5 min. Recorded USVs were analyzed as previously described [81]. Briefly, Avisoft SASLab Pro software (RRID:SCR\_014438) was used to analyze USVs. Signals were filtered from 1 to 100 kHz and digitized with a sampling frequency of 250 kHz and 16 bits per sample (Avisoft UltraSoundGate 116H). To generate spectrograms, the following parameters were used: FFT length: 256, frame size: 100, window: FlatTop, overlap: 75%, resulting in a frequency resolution of 977 Hz and a temporal resolution of 0.256 ms. USV frequencies lower than 45 kHz were filtered out to reduce background white noises.

### Three-chamber test

The size of the three-chambered apparatus was 40 cm W  $\times$  20 cm H  $\times$  26 cm D with a center chamber of 12 cm W and side chambers of 14 cm W. In the first session, a subject mouse could freely move around the whole three-chambered apparatus with 2 small plastic containers in the left or right corners for 10 min (Session 1). The mouse was then gently confined in the center chamber while a novel “Object” and a WT stranger mouse “Stranger 1 (129Sv strain)”

was placed in the 2 plastic containers. The subject mouse was then allowed to freely explore all 3 chambers for 10 min (Session 2). In the third session, the subject mouse was again gently guided to the center chamber while the “Object” was replaced with a WT “Stranger 2” mouse. The subject mouse again freely explored all 3 chambers for 10 min (Session 3). Object/Stranger exploration was defined by the mouse’s nose being oriented toward the target and coming within 2 cm of it as measured by EthoVision XT 12 program (Noldus).

### Direct interaction test

For the direct interaction test between mice in the same genetic background (C57BL/6J), each mouse was first habituated in a direct social interaction box for 30 min on the day before experiment. On the test day, pairs of mice of the same ages and genotypes, which have not met before, were placed in a direct interaction box, and their interactions were recorded for 10 min. For the direct interaction test between mice in different genetic backgrounds (C57BL/6J and C3H/HeJ), WT or *Katnal2*-KO males in the C57BL/6J background were paired with age/weight-matched non-familiar C3H/HeJ males (Jackson Labs). Each subject mouse and C3H/HeJ partner were placed in the direct social interaction box and allowed to freely interact for 10 min. Social interactions were recorded using a top-view camera and quantified manually by trained researchers in a blind manner using the Premiere Pro 2020 program (Adobe). The behaviors from the unidirectional social interaction test were grouped into 2 categories: reciprocal social interaction where one mouse socially explores the other and the other animal reciprocates the social interaction; nonreciprocal interaction where social actions of *Katnal2*-KO mouse were not reciprocated by the C3H/HeJ partner.

### Open-field test

Mice were placed in an open-field box (40 × 40 × 40 cm) and recorded with a video camera for 60 min. The center zone line was 10 cm apart from the edge. The testing room was illuminated at approximately 0 lux. Mice movements were analyzed using EthoVision XT 12 program (Noldus).

### Rotarod test

Mice were placed on the rotating rod for 10 s, followed by the start of rod rotation. The rotating speed of the rod was gradually increased from 4 to 40 rpm over 5 min. The assay was performed for 5 consecutive days while measuring the latencies of mice falling from the rod or showing 360-degree rotation on the rod.

### Elevated plus maze

The elevated plus maze consisted of 2 open arms, 2 closed arms, and a center zone, and was elevated to a height of 50 cm above the floor. Mice were placed in the center zone and allowed to explore the space for 8 min. The data was manually quantified by trained researchers in a blind manner.

### Light-dark chamber test

The light-dark test apparatus consisted of light (approximately 400 lux) and dark (approximately 0 lux) chambers that adhered to each other. The size of the light chamber was 20 × 30 × 20 cm, and that of the dark chamber was 20 × 13 × 20 cm. An entrance enabled mice to freely move across the light and dark chambers. Mice were introduced to the center of the light chamber and allowed to explore the apparatus freely for 5 min. The time spent in dark and

light chambers and transition frequencies were measured using EthoVision XT 10 program (Noldus).

### Novel object recognition test

The novel object recognition test was performed in the open-field box. On the day after the open-field test, mice were allowed to freely explore 2 identical objects (blue cylinder or silver-colored box) in the open-field box for 20 min. Twenty-four hours later, mice were placed in the same box where one of the 2 objects was replaced with a new one. Sniffing time for each object was measured. Object exploration was defined by the mouse's nose being oriented toward the object and coming within 2 cm of it as measured by EthoVision XT 12 program (Noldus).

### Morris water maze

Mice were trained to find the hidden platform (10-cm diameter) in a white plastic tank (120-cm diameter). Mice were given 3 trials per day with an inter-trial interval of 30 min. The learning-phase experiments of the water maze were performed for 7 consecutive days, followed by the probe test on day 8 where mice were given 1 min to find the removed platform. For reversal training (days 9 to 13), the location of the platform was switched to the opposite position from the previously trained quadrant, and mice were trained to learn the new position of the platform. Target quadrant occupancy and the exact number of crossings over the former platform location during the probe test were measured using EthoVision XT 12 program (Noldus).

### Acoustic startle

Acoustic startle responses were measured to determine auditory functions. After 5 minutes of 65-dB background acclimation in the acoustic startle apparatus (San Diego Instrument; SR-Lab ABS system #2325-0400), 92 of 40-ms acoustic stimulus (7 each for 70~120 dB with 5-dB intervals; 7 mock trials; 8 of 120 dB trials located 4 each at the beginning and the end) were given to subject mice in pseudorandomized order. The startle responses were recorded and analyzed using the SR-LAB software (San Diego Instrument).

### Contextual fear conditioning test

Subject mice were introduced to the fear-conditioning box (Coulbourn Instrument; H13-16) for 10 min and allowed to freely explore the box a day before the day of the experiment. On the conditioning day, mice were placed in the same box (20 lux; grid floor). After 2 min of acclimation, 3 electric foot shocks (0.5 mA, 2 s) were delivered at 1 min intervals. After 3 min of the post-shock period, mice were returned to home cages. Twenty-four hours after, mice were placed in the fear box with the same condition to monitor behaviors for 3 min. This monitoring experiment was repeated 7 days after the conditioning. A top-view camera was to record mouse movements, which were analyzed using the ActiMetrics FreezeFrame 3 software (freezing threshold = 10%).

### Immunohistochemistry

Mouse brain slices (50  $\mu$ m; vibratome, Leica) were prepared and stained with DAPI-containing Vectashield (Vector Laboratory) and for Cux1 and FoxP2 using the following commercial antibodies: Cux1 (Santa Cruz sc-13024 at 1:500) and FoxP2 (Abcam ab16046 at 1:500).

## Immunocytochemistry

Cultured hippocampal neurons (DIV 7) were fixed in 4% PFA/4% sucrose-containing Tyrode's solution (119 mM NaCl, 2.5 mM KCl, 2 mM CaCl<sub>2</sub>, 2 mM MgCl<sub>2</sub>, 25 mM HEPES, 30 mM glucose (pH 7.4)) for 15 min, permeabilized in 0.25% Triton X-100 in Tyrode's solution for 5 min, and then blocked in 5% Normal Donkey Serum (NDS)-containing Tyrode's solution at 37°C for 30 min. Then, tissues were treated with primary antibodies (anti-Arl13b (Proteintech 17711-1-AP, 1:1000); anti-NeuN (EMD Millipore ABN90, 1:1,000)) containing Tyrode's solution with 5% NDS at 37°C for 2 h and secondary antibodies (1:1,000) for 45 min. The length of primary cilia was measured by ImageJ software (fiji-win64).

## X-gal staining

X-gal staining for *Katnal2*- $\beta$ -galactosidase fusion proteins was performed using brain slices (100- $\mu$ m coronal sections) from *Katnal2*-KO cassette-containing mice (MAE-4330; *Katnal2*<sup>tm1a(EUCOMM)Wtsi</sup>; P21 and P56) and X-gal staining (20 mg/ml X-gal; in 2 mM MgCl<sub>2</sub>, 5 mM K<sub>4</sub>Fe(CN)<sub>6</sub>·3H<sub>2</sub>O (Sigma #P-8131), 5 mM K<sub>3</sub>Fe(CN)<sub>6</sub>, 0.01% DOC, 0.02% NP-40 in 1 $\times$  PBS).

## CSF drainage assay

To check the CSF drainage to the deep cervical lymph node, the head of anesthetized mice was fixed on the stereotaxic frame, and 1  $\mu$ l of Alexa Fluor 488-conjugated ovalbumin (Invitrogen O34781) was injected for 5 min in the lateral ventricle. The detailed coordinate is the following: AP = 0.0; ML = -1.2; DV = -2.4 from Bregma. After 3-min break, the injection needle was removed. After recovery for an hour on the 37°C heating pad, injected mice were cardiac perfused with Heparin-containing PBS/PFA, dCLNs were dissected out and cryoprotected in 15%/30% serial. The lymph nodes were prepared into 40- $\mu$ m sections by using cryostat, and costained with DAPI, and imaged using LSM-780 (Zeiss). The coverage of OVA-488 and DAPI of the lymph nodes were measured by ImageJ program (fiji-win64).

## Statistics

For group comparisons, Student's *t* test or Mann-Whitney test was used based on the results of normality testing using D'Agostino & Pearson or Shapiro-Wilk normality test. The Mann-Whitney test was used for any column that yielded a *p* value < 0.05 in either normality test. For multi-comparisons with 2 independent variables, two-way ANOVA and Sidak's multiple comparison test were used. For relative brain regional volumes/CBV, adjusted *p* values from one-sample *t* test were used. For ciliary beating frequencies, we used a permutation test with 10,000 iterations (MATLAB). For the comparison of 3 groups with the 1 independent variable (rescue experiment), we used one-way ANOVA with Dunnett's post hoc test. GraphPad Prism 7 was used for statistical analyses. See [S1 Data](#) for statistical details.

## Supporting information

**S1 Fig. Gene knockout strategy for *Katnal2*-KO mice.** (A) Domain structure of the *Katnal2* protein (539 aa-long), known sites of ASD patient-derived point mutations (49 variants from 14 reports), and the protein regions corresponding to exon 3, which was deleted in *Katnal2*-KO mice (55 aa in the LisH domain). LisH domain, lissencephaly-1 homology domain; AAA-ATPase domain, AAA family ATPase domain. (B) *Katnal2* knockout (KO) strategy in mice. The same primer sets are used to detect WT and mutant PCR products (259 and 215 base pairs); they differ by the presence or absence of exon 3, deletion of which leads to a shift



in the open-reading frame. (C) PCR genotyping for WT, heterozygous *Katnal2*-KO (HT), and homozygous *Katnal2*-KO (KO) mice (postnatal day [P56]). (D) Validation of *Katnal2* KO by immunoblot analysis; we used mouse testis samples (P56) instead of brain samples because the expression levels of *Katnal2* protein are much greater in the testis relative to the brain. In the brain, *Katnal2* expression is confined to select brain regions and cell types, such as ependymal cells lining ventricular walls, as shown by X-gal staining (see **Figs 2A and S5**). Note also that there is a major *Katnal2* protein band (approximately 45 kDa; arrowhead) in WT but not KO testis samples, as revealed by immunostaining with *Katnal2* polyclonal antibodies (#2817) raised against aa 517–539 of the *Katnal2* protein. Asterisk indicates a nonspecific band recognized by *Katnal2* antibodies. (E) Normal body weights in *Katnal2*-KO mice (2 months). ( $n = 7$  mice [WT], 9 mice [KO], Student's *t* test). (F and G) Normal superficial (layer 2/3) and deep (layer 6) cortical layer structures in the *Katnal2*-KO brain (P56), as revealed by double immunofluorescence staining for NeuN (a neuronal marker) and *Cux1* (layer 2/3 marker) or for NeuN and *FoxP2* (layer 6). DAPI staining was performed for nuclear staining. The examples shown here are from the somatosensory cortex (layers 1–6). (H) Sholl analysis of CA1 hippocampal neurons from WT and *Katnal2*-KO mice, visualized by cross-breeding with *Thy1*-EGFP mice. (P21–23;  $n = 19$  cells from 6 [WT], 19, 6 [KO], two-way RM-ANOVA). (I) Comparable lengths of the primary cilia in cultured hippocampal neurons (days in vitro 7) from WT and *Katnal2*-KO embryos. ( $n = 147$  images from 11 glass slides from 4 mice [WT], 165, 11, 4 [KO], Student's *t* test). Data values represent means  $\pm$  SEM. Significance is indicated as ns (not significant). Statistical results and numerical data values can be found in **S1 Data**. Full-length PCR and immunoblot images can be found in **S1 Raw Images**. (TIF)

**S2 Fig. Abnormal social communication and mounting in *Katnal2*-KO mice.** (A) Normal levels of social approach and social novelty recognition in *Katnal2*-KO mice (2–3 months; male) in the three-chamber test, as shown by time spent sniffing social and object targets (S1/S2, old/new social target; O, object), time spent in the chamber, and the preference index (time difference for S1–O [S2 – S1] / total time  $\times$  100). ( $n = 17$  mice [WT], 16 [KO], two-way RM-ANOVA [sniffing time, chamber time], Student's *t*-test [sociability index, social novelty recognition index]). (B) Normal levels of direct social interaction in *Katnal2*-KO mice (2–3 months) in the direct social interaction test, wherein freely moving WT/mutant mouse pairs were used to measure nose-to-nose, nose-to-tail, and following. ( $n = 11$  pairs [WT], 13 [KO], two-way RM-ANOVA). (C) Normal levels of social interaction in *Katnal2*-KO mice (2–3 months) in a modified version of the direct social interaction test, where a subject mouse interacted with a stranger mouse of C3H background (i.e., with a different coat color) and unidirectional and bidirectional/reciprocal social interactions were measured. ( $n = 10$  mice [WT], 11 [KO], two-way RM-ANOVA). (D) Increased courtship USVs upon encountering a novel female stranger mouse is seen for *Katnal2*-KO male mice (2–3 months), as indicated by USV call frequency and duration (total and each call). ( $n = 19$  [WT], 22 [KO], Student's *t* test [frequency, each-call duration], Mann–Whitney test [total duration]). (E) Largely normal social interactions during the courtship tests, except for mounting, as shown by analysis of male-to-female social interactions (nose-to-nose, nose-to-tail, following), female-to-male interactions (nose-to-nose, nose-to-tail, following), bidirectional interactions (dyadic), and mounting. Mounting behaviors alone show a genotype-related difference, as determined by Student's *t* test. Two-way ANOVA encompassing all behaviors did not reveal a genotype-related difference. ( $n = 12$  [WT], 14 [KO], two-way RM-ANOVA). (F) Decreased mounting success in *Katnal2*-KO male mice (2–3 months), as shown by the proportion of mice that succeeded in mounting during a courtship-test session (5 min). ( $n = 15$  [WT], 20 [KO], Chi-square test). (G) Normal repetitive self-

grooming in *Katnal2*-KO mice (2–3 months) in a new home cage without bedding. ( $n = 13$  [WT], 17 [KO], Student's  $t$  test). Data values represent means  $\pm$  SEM. Significance is indicated as \* ( $<0.05$ ), \*\* ( $<0.01$ ), \*\*\* ( $<0.001$ ) or ns (not significant). Statistical results and numerical data values can be found in [S1 Data](#).

(TIF)

**S3 Fig. Normal levels of locomotion, anxiety-like behavior, acoustic startle, motor coordination, and learning and memory in *Katnal2*-KO mice.** (A) Normal levels of locomotor activity in the open-field test for *Katnal2*-KO mice (2–3 months), as shown by distance moved. Note that there is no genotype-related difference in the time spent in the center region of the open-field area, suggestive of normal anxiety-like behavior in the mutant mice. ( $n = 18$  mice [WT], 21 [KO], two-way RM-ANOVA [distance moved and time in center], Mann-Whitney test [total distance moved], Student's  $t$  test [total time in center]). (B) Normal levels of anxiety-like behavior in the elevated plus-maze for *Katnal2*-KO mice (2–3 months), as shown by % time spent in open arms. ( $n = 18$  [WT], 22 [KO], Student's  $t$  test). (C) Normal levels of anxiety-like behavior in the light-dark test for *Katnal2*-KO mice (2–3 months), as shown by time in the light box. ( $n = 12$  [WT], 16 [KO], Student's  $t$  test). (D) Normal levels of acoustic startle for *Katnal2*-KO mice (2–3 months). ( $n = 9$  [WT], 7 [KO], two-way RM-ANOVA). (E) Normal levels of motor coordination and learning in the rotarod test in *Katnal2*-KO mice (2–3 months), as shown by the latency to fall. ( $n = 17$  [WT], 15 [KO], two-way RM-ANOVA). (F) Normal levels of learning and memory in the forward and reversal phases of the Morris water maze test in *Katnal2*-KO mice (2–3 months). ( $n = 12$  [WT], 15 [KO], two-way RM-ANOVA [escape latency, time in quadrant in probe test and reverse probe test], Mann-Whitney test [crossing number], Student's  $t$  test [crossing number (reversal)]). (G) Normal levels of object recognition memory in the novel object recognition test in *Katnal2*-KO mice (2–3 months), as shown by the novel-object preference (% time spent exploring the novel object). ( $n = 13$  [WT], 10 [KO], Student's  $t$  test). (H) Normal levels of learning and memory in the contextual fear memory test in *Katnal2*-KO mice (2–3 months), as shown by freezing levels during fear acquisition, at 24-h retrieval, and at subsequent 8-day retrieval. ( $n = 18$  [WT], 15 [KO], two-way RM-ANOVA). Data values represent means  $\pm$  SEM. Significance is indicated as ns (not significant). Statistical results and numerical data values can be found in [S1 Data](#).

(TIF)

**S4 Fig. Moderately increased ventricular areas in P7 *Katnal2*-KO mice and largely normal intracranial brain volumes in P70 *Katnal2*-KO mice.** (A) Moderately increased areas of lateral ventricles in *Katnal2*-KO mice at P7, as shown by measurements derived from coronal brain slices. Note that brain areas are not increased at P7. AP axis, anterior-posterior axis. Scale bar, 2 mm. ( $n = 5$  mice [WT], 6 [KO], two-way RM-ANOVA). (B) Largely normal intracranial brain volumes, with very moderate increases in select brain regions, among *Katnal2*-KO mice (3 months), as shown by MRI analyses of absolute and relative brain volumes (two-way ANOVA). Note, however, that there are moderate *Katnal2*-KO-dependent increases in some brain regions (one-sample  $t$  test). ( $n = 8$  mice [WT], 6 [KO], two-way RM-ANOVA and one-sample  $t$  test). Significance is indicated as \* ( $<0.05$ ) or ns (not significant). Statistical results and numerical data values can be found in [S1 Data](#).

(TIF)

**S5 Fig. Distribution patterns of *Katnal2* proteins in the mouse brain, as revealed by X-gal staining.** (A and B) Distribution patterns of *Katnal2* proteins in the mouse brain, as revealed by X-gal staining of *Katnal2*- $\beta$ -galactosidase fusion proteins expressed in *Katnal2*-KO mice

(P21 and P56) with the  $\beta$ -geo cassette unremoved. Scale bar, 1 mm.  
(TIF)

**S6 Fig. Additional examples of SEM images used to determine ependymal ciliary length.**

(A and B) Additional examples of SEM images from the lateral ventricles of WT and *Katnal2*-KO mice (P28-33; 6 images from 6 WT mice and 11 images from 11 KO mice).

(TIF)

**S7 Fig. Comparison of CBVs in different brain regions of WT and *Katnal2*-KO mice.**

(A) Comparisons of cerebral blood volumes (CBVs) in WT and *Katnal2*-KO brains, as shown by the extents of decreases in fMRI signals induced by hypoxic nitrogen stimulus in different brain regions (left, relative CBVs) and the KO values normalized to WT values (right, %WT). Iso-cortex includes somatomotor area, somatosensory area, gustatory area, visceral area, auditory area, visual area, anterior cingulate area, prelimbic area, infralimbic area, orbital area, agranular insular area, retrosplenial area, posterior parietal association, temporal association area, perirhinal area, and entorhinal area. ( $n = 8$  mice [WT], 6 [KO], two-way ANOVA and one-sample  $t$  test). (B) Comparable levels of relative CBVs (BOLD signals) in lateral ventricles containing the choroid plexus region in WT and *Katnal2*-KO mice, as assessed by hypoxic nitrogen stimulus. The red-colored areas indicate representative choroid plexus-containing voxels that we used for the signal tracing. ( $n = 9$  mice [WT], 9 [KO], Mann-Whitney test). (C) Minimal levels of relative CBVs (BOLD signals) in lateral ventricles without the choroid plexus region in WT and *Katnal2*-KO mice, indicating that the majority of BOLD signals in lateral ventricles are from the choroid plexus and that the effect of the CSF-containing region on BOLD signals is minimal. The yellow-colored areas indicate representative choroid plexus-non-containing lateral ventricle voxels that we used for the signal tracing. (D) Lack of genotype differences in the levels of ion co-transporters (Anion Exchanger 2/AE2 and  $\text{Na}^+/\text{K}^+$ -ATPase subunit  $\alpha 1$ ) and water channels (aquaporin-1/AQP-1 Student's  $t$ -test), as shown by immunoblot analysis of choroid plexus lysates from WT and *Katnal2*-KO mice ( $n = 6$  samples [WT], 5 [KO]; 4 choroid plexus samples from 2 mice were pooled to make  $n$  of 1). (E) Experimental scheme for the measurement of CSF drainage. Fluorescent ovalbumin proteins (OVA-488) were introduced by intracerebroventricular (icv) injection into the lateral ventricles of WT and *Katnal2*-KO mice (2 months), and signals were measured in the deep cervical lymph nodes (dCLNs). (F) Example images and quantification of fluorescent ovalbumin proteins detected in the dCLNs outside the brain. DAPI staining was performed to label cells. Scale bar, 100  $\mu\text{m}$ . ( $n = 3$  mice [WT], 5 [KO], Mann-Whitney test). Data values represent means  $\pm$  SEM. Significance is indicated as \* ( $<0.05$ ), \*\* ( $<0.01$ ), or ns (not significant). Statistical results and numerical data values can be found in [S1 Data](#). Full-length immunoblot images can be found in [S1 Raw Images](#).

(TIF)

**S8 Fig. Volcano plots of DEGs for P21-*Katnal2*/WT and P70-*Katnal2* transcripts.**

(A and B) Volcano plots of differentially expressed genes (DEGs) from P21- and P70-*Katnal2*/WT transcripts, shown together with the lists of top-ranked DEGs, sorted by  $p$  values. ( $n = 5$  mice for WT and KO, FDR  $< 0.05$  and fold-change  $> 1.5$ -fold). Detailed DEG results can be found in [S3 Data](#).

(TIF)

**S1 Data. Statistical details and numerical values.**

(XLSX)

**S2 Data. Total RNA-Seq results.**

(XLSX)

**S3 Data. DEGs from P21-Katnal2/WT and P70-Katnal2 transcripts.**

(XLSX)

**S4 Data. GSEA results for P21-Katnal2/WT and P70-Katnal2 transcripts.**

(XLSX)

**S5 Data. Lists of gene sets and genes in each gene sets used in the present study.**

(XLSX)

**S1 Raw Images. Full-length images of immunoblotting and PCR experiments.**

(PPTX)

**S1 Movie. An example of ependymal ciliary beating movements.** An example of ependymal ciliary beatings observed in lateral ventricles of WT mice (P28-42). The movie was generated using images acquired at approximately 1,000 frames/sec.

(MP4)

## Acknowledgments

We would like to thank Dr. Ji-Seon Seo for helpful comments, the facilities and the scientific and technical assistance of the EM & Histology Core Facility, and Dr. Yongsuk Hur at the Bio-Medical Research Center, KAIST.

## Author Contributions

**Conceptualization:** Ryeonghwa Kang, Kyungdeok Kim, Eunjoon Kim.

**Data curation:** Ryeonghwa Kang, Kyungdeok Kim, Miram Shin, Kwangmin Ryu, Subin Choi, Esther Yang, Wangyong Shin, Seungjoon Lee, Suho Lee, Zachary Papadopoulos, Ji Hoon Ahn.

**Formal analysis:** Ryeonghwa Kang, Kyungdeok Kim, Yewon Jung, Hyojin Kang.

**Funding acquisition:** Eunjoon Kim.

**Investigation:** Ryeonghwa Kang, Kyungdeok Kim, Yewon Jung, Sang-Han Choi, Chanhee Lee, Geun Ho Im, Miram Shin, Kwangmin Ryu, Subin Choi, Esther Yang, Wangyong Shin, Ji Hoon Ahn.

**Methodology:** Seungjoon Lee.

**Supervision:** Gou Young Koh, Hyun Kim, Won-Ki Cho, Soochul Park, Seong-Gi Kim, Eunjoon Kim.

**Visualization:** Ryeonghwa Kang, Kyungdeok Kim.

**Writing – original draft:** Ryeonghwa Kang, Kyungdeok Kim, Eunjoon Kim.

**Writing – review & editing:** Gou Young Koh, Jonathan Kipnis, Hyun Kim, Won-Ki Cho, Soochul Park, Seong-Gi Kim.

## References

1. Williams CA, Dagli A, Battaglia A. Genetic disorders associated with macrocephaly. *Am J Med Genet A*. 2008; 146A(15):2023–37. Epub 2008/07/17. <https://doi.org/10.1002/ajmg.a.32434> PMID: 18629877.

2. Lainhart JE, Piven J, Wzorek M, Landa R, Santangelo SL, Coon H, et al. Macrocephaly in children and adults with autism. *J Am Acad Child Adolesc Psychiatry*. 1997; 36(2):282–290. <https://doi.org/10.1097/00004583-199702000-00019> PMID: 9031582.
3. Pan PY, Bolte S, Kaur P, Jamil S, Jonsson U. Neurological disorders in autism: A systematic review and meta-analysis. *Autism*. 2020;1362361320951370. Epub 2020/09/11. <https://doi.org/10.1177/1362361320951370> PMID: 32907344.
4. Shen MD, Nordahl CW, Li DD, Lee A, Angkustsiri K, Emerson RW, et al. Extra-axial cerebrospinal fluid in high-risk and normal-risk children with autism aged 2–4 years: a case-control study. *Lancet Psychiatry*. 2018; 5(11):895–904. Epub 20180927. [https://doi.org/10.1016/S2215-0366\(18\)30294-3](https://doi.org/10.1016/S2215-0366(18)30294-3) PMID: 30270033; PubMed Central PMCID: PMC6223655.
5. Tully HM, Dobyns WB. Infantile hydrocephalus: a review of epidemiology, classification and causes. *Eur J Med Genet*. 2014; 57(8):359–68. Epub 2014/06/17. <https://doi.org/10.1016/j.ejmg.2014.06.002> PMID: 24932902; PubMed Central PMCID: PMC4334358.
6. Kahle KT, Kulkarni AV, Limbrick DD Jr, Warf BC. Hydrocephalus in children. *Lancet*. 2016; 387(10020):788–99. Epub 2015/08/11. [https://doi.org/10.1016/S0140-6736\(15\)60694-8](https://doi.org/10.1016/S0140-6736(15)60694-8) PMID: 26256071.
7. Del Bigio MR. Ependymal cells: biology and pathology. *Acta Neuropathol*. 2010; 119(1):55–73. Epub 2009/12/22. <https://doi.org/10.1007/s00401-009-0624-y> PMID: 20024659.
8. Kishimoto N, Sawamoto K. Planar polarity of ependymal cilia. *Differentiation*. 2012; 83(2):S86–90. Epub 2011/11/22. <https://doi.org/10.1016/j.diff.2011.10.007> PMID: 22101065.
9. Kousi M, Katsanis N. The Genetic Basis of Hydrocephalus. *Annu Rev Neurosci*. 2016; 39:409–35. Epub 20160502. <https://doi.org/10.1146/annurev-neuro-070815-014023> PMID: 27145913.
10. Norris DP, Grimes DT. Mouse models of ciliopathies: the state of the art. *Dis Model Mech*. 2012; 5(3):299–312. <https://doi.org/10.1242/dmm.009340> PMID: 22566558; PubMed Central PMCID: PMC3339824.
11. Del Bigio MR. The ependyma: a protective barrier between brain and cerebrospinal fluid. *Glia*. 1995; 14(1):1–13. <https://doi.org/10.1002/glia.440140102> PMID: 7615341.
12. Sotak BN, Gleeson JG. Can't get there from here: cilia and hydrocephalus. *Nat Med*. 2012; 18(12):1742–1743. <https://doi.org/10.1038/nm.3011> PMID: 23223060.
13. Kapitein LC, Hoogenraad CC. Building the Neuronal Microtubule Cytoskeleton. *Neuron*. 2015; 87(3):492–506. <https://doi.org/10.1016/j.neuron.2015.05.046> PMID: 26247859.
14. Willsey HR, Walentek P, Exner CRT, Xu Y, Lane AB, Harland RM, et al. Katanin-like protein *Katnal2* is required for ciliogenesis and brain development in *Xenopus* embryos. *Dev Biol*. 2018; 442(2):276–87. Epub 20180808. <https://doi.org/10.1016/j.ydbio.2018.08.002> PMID: 30096282; PubMed Central PMCID: PMC6143417.
15. Ververis A, Christodoulou A, Christoforou M, Kamilari C, Lederer CW, Santama N. A novel family of katanin-like 2 protein isoforms (KATNAL2), interacting with nucleotide-binding proteins Nubp1 and Nubp2, are key regulators of different MT-based processes in mammalian cells. *Cell Mol Life Sci*. 2016; 73(1):163–84. Epub 20150708. <https://doi.org/10.1007/s00018-015-1980-5> PMID: 26153462.
16. Tu F, Sedzinski J, Ma Y, Marcotte EM, Wallingford JB. Protein localization screening in vivo reveals novel regulators of multiciliated cell development and function. *J Cell Sci*. 2018; 131(3). Epub 20180129. <https://doi.org/10.1242/jcs.206565> PMID: 29180514; PubMed Central PMCID: PMC5826043.
17. Cheung K, Senese S, Kuang J, Bui N, Ongpipattanukul C, Gholkar A, et al. Proteomic Analysis of the Mammalian Katanin Family of Microtubule-severing Enzymes Defines Katanin p80 subunit B-like 1 (KATNBL1) as a Regulator of Mammalian Katanin Microtubule-severing. *Mol Cell Proteomics*. 2016; 15(5):1658–69. Epub 20160229. <https://doi.org/10.1074/mcp.M115.056465> PMID: 26929214; PubMed Central PMCID: PMC4858946.
18. Dunleavy JEM, Okuda H, O'Connor AE, Merriner DJ, O'Donnell L, Jamsai D, et al. Katanin-like 2 (KATNAL2) functions in multiple aspects of haploid male germ cell development in the mouse. *PLoS Genet*. 2017; 13(11):e1007078. Epub 20171114. <https://doi.org/10.1371/journal.pgen.1007078> PMID: 29136647; PubMed Central PMCID: PMC5705150.
19. Wei X, Liu W, Zhu X, Li Y, Zhang X, Chen J, et al. Biallelic mutations in KATNAL2 cause male infertility due to oligo-astheno-teratozoospermia. *Clin Genet*. 2021; 100(4):376–85. Epub 20210611. <https://doi.org/10.1111/cge.14009> PMID: 34096614.
20. Zheng J, Long F, Cao X, Xiong B, Li Y. Knockout of *Katnal2* Leads to Autism-like Behaviors and Developmental Delay in Zebrafish. *Int J Mol Sci*. 2022; 23(15). Epub 20220729. <https://doi.org/10.3390/ijms23158389> PMID: 35955524; PubMed Central PMCID: PMC9368773.
21. Williams MR, Fricano-Kugler CJ, Getz SA, Skelton PD, Lee J, Rizzuto CP, et al. A Retroviral CRISPR-Cas9 System for Cellular Autism-Associated Phenotype Discovery in Developing Neurons. *Sci Rep*.

- 2016; 6:25611. <https://doi.org/10.1038/srep25611> PMID: 27161796; PubMed Central PMCID: PMC4861960.
22. O'Roak BJ, Vives L, Girirajan S, Karakoc E, Krumm N, Coe BP, et al. Sporadic autism exomes reveal a highly interconnected protein network of de novo mutations. *Nature*. 2012; 485(7397):246–50. Epub 2012/04/13. <https://doi.org/10.1038/nature10989> [pii]10.1038/nature10989. PMID: 22495309.
  23. De Rubeis S, He X, Goldberg AP, Poultney CS, Samocha K, Cicek AE, et al. Synaptic, transcriptional and chromatin genes disrupted in autism. *Nature*. 2014; 515(7526):209–215. <https://doi.org/10.1038/nature13772> PMID: 25363760; PubMed Central PMCID: PMC4402723.
  24. Wang T, Hoekzema K, Vecchio D, Wu H, Sulovari A, Coe BP, et al. Large-scale targeted sequencing identifies risk genes for neurodevelopmental disorders. *Nat Commun*. 2020; 11(1):4932. Epub 2020/10/03. <https://doi.org/10.1038/s41467-020-18723-y> PMID: 33004838; PubMed Central PMCID: PMC7530681.
  25. Yuen RK, Thiruvahindrapuram B, Merico D, Walker S, Tammimies K, Hoang N, et al. Whole-genome sequencing of quartet families with autism spectrum disorder. *Nat Med*. 2015; 21(2):185–191. <https://doi.org/10.1038/nm.3792> PMID: 25621899.
  26. Ruzzo EK, Perez-Cano L, Jung JY, Wang LK, Kashef-Haghighi D, Hartl C, et al. Inherited and De Novo Genetic Risk for Autism Impacts Shared Networks. *Cell*. 2019; 178(4):850–66 e26. <https://doi.org/10.1016/j.cell.2019.07.015> PMID: 31398340; PubMed Central PMCID: PMC7102900.
  27. Stessman HA, Xiong B, Coe BP, Wang T, Hoekzema K, Fenckova M, et al. Targeted sequencing identifies 91 neurodevelopmental-disorder risk genes with autism and developmental-disability biases. *Nat Genet*. 2017; 49(4):515–526. <https://doi.org/10.1038/ng.3792> PMID: 28191889; PubMed Central PMCID: PMC5374041.
  28. Sanders SJ, Murtha MT, Gupta AR, Murdoch JD, Raubeson MJ, Willsey AJ, et al. De novo mutations revealed by whole-exome sequencing are strongly associated with autism. *Nature*. 2012; 485(7397):237–41. Epub 2012/04/13. <https://doi.org/10.1038/nature10945> PMID: 22495306.
  29. Guo H, Wang T, Wu H, Long M, Coe BP, Li H, et al. Inherited and multiple de novo mutations in autism/developmental delay risk genes suggest a multifactorial model. *Mol Autism*. 2018; 9:64. Epub 2018/12/20. <https://doi.org/10.1186/s13229-018-0247-z> PMID: 30564305; PubMed Central PMCID: PMC6293633.
  30. Feng G, Mellor RH, Bernstein M, Keller-Peck C, Nguyen QT, Wallace M, et al. Imaging neuronal subsets in transgenic mice expressing multiple spectral variants of GFP. *Neuron*. 2000; 28(1):41–51. [https://doi.org/10.1016/s0896-6273\(00\)00084-2](https://doi.org/10.1016/s0896-6273(00)00084-2) PMID: 11086982.
  31. Anvarian Z, Mykytyn K, Mukhopadhyay S, Pedersen LB, Christensen ST. Cellular signalling by primary cilia in development, organ function and disease. *Nat Rev Nephrol*. 2019; 15(4):199–219. <https://doi.org/10.1038/s41581-019-0116-9> PMID: 30733609; PubMed Central PMCID: PMC6426138.
  32. Wolburg H, Paulus W. Choroid plexus: biology and pathology. *Acta Neuropathol*. 2010; 119(1):75–88. Epub 2009/12/24. <https://doi.org/10.1007/s00401-009-0627-8> PMID: 20033190.
  33. Hagenlocher C, Walentek P, Ller CM, Thumberger T, Feistel K. Ciliogenesis and cerebrospinal fluid flow in the developing *Xenopus* brain are regulated by *foxf1*. *Cilia*. 2013; 2(1):12. Epub 2013/09/24. <https://doi.org/10.1186/2046-2530-2-12> PMID: 24229449; PubMed Central PMCID: PMC3848805.
  34. Mohammed BJ, Mitchell TJ, Andrew PW, Hirst RA, O'Callaghan C. The effect of the pneumococcal toxin, pneumolysin on brain ependymal cilia. *Microb Pathog*. 1999; 27(5):303–309. <https://doi.org/10.1006/mpat.1999.0306> PMID: 10547234.
  35. Hirst RA, Rutman A, Sikand K, Andrew PW, Mitchell TJ, O'Callaghan C. Effect of pneumolysin on rat brain ciliary function: comparison of brain slices with cultured ependymal cells. *Pediatr Res*. 2000; 47(3):381–384. <https://doi.org/10.1203/00006450-200003000-00016> PMID: 10709739.
  36. van Pee K, Mulvihill E, Muller DJ, Yildiz O. Unraveling the Pore-Forming Steps of Pneumolysin from *Streptococcus pneumoniae*. *Nano Lett*. 2016; 16(12):7915–24. Epub 2016/11/03. <https://doi.org/10.1021/acs.nanolett.6b04219> PMID: 27796097.
  37. van Pee K, Neuhaus A, D'Imprima E, Mills DJ, Kuhlbrandt W, Yildiz O. CryoEM structures of membrane pore and prepore complex reveal cytolytic mechanism of Pneumolysin. *elife*. 2017; 6. Epub 2017/03/21. <https://doi.org/10.7554/eLife.23644> PMID: 28323617; PubMed Central PMCID: PMC5437283.
  38. Guirao B, Meunier A, Mortaud S, Aguilar A, Corsi J-M, Strehl L, et al. Coupling between hydrodynamic forces and planar cell polarity orients mammalian motile cilia. *Nat Cell Biol*. 2010; 12(4):341–350. <https://doi.org/10.1038/ncb2040> PMID: 20305650
  39. Coletti AM, Singh D, Kumar S, Shafin TN, Briody PJ, Babbitt BF, et al. Characterization of the ventricular-subventricular stem cell niche during human brain development. *Development*. 2018; 145(20). Epub 2018/10/26. <https://doi.org/10.1242/dev.170100> PMID: 30237244; PubMed Central PMCID: PMC6215394.

40. Ohata S, Alvarez-Buylla A. Planar Organization of Multiciliated Ependymal (E1) Cells in the Brain Ventricular Epithelium. *Trends Neurosci.* 2016; 39(8):543–51. Epub 2016/06/18. <https://doi.org/10.1016/j.tins.2016.05.004> PMID: 27311928; PubMed Central PMCID: PMC5312752.
41. Del Bigio MR. Neuropathological changes caused by hydrocephalus. *Acta Neuropathol.* 1993; 85(6):573–585. <https://doi.org/10.1007/BF00334666> PMID: 8337936.
42. Del Bigio MR. Neuropathology and structural changes in hydrocephalus. *Dev Disabil Res Rev.* 2010; 16(1):16–22. <https://doi.org/10.1002/ddrr.94> PMID: 20419767.
43. Tsubokawa T, Katayama Y, Kawamata T. Impaired hippocampal plasticity in experimental chronic hydrocephalus. *Brain Inj.* 1988; 2(1):19–30. <https://doi.org/10.3109/02699058809150929> PMID: 2844349.
44. Lee D, Le TT, Im GH, Kim SG. Whole-brain perfusion mapping in mice by dynamic BOLD MRI with transient hypoxia. *J Cereb Blood Flow Metab.* 2022; 42(12):2270–86. Epub 20220728. <https://doi.org/10.1177/0271678X221117008> PMID: 35903000; PubMed Central PMCID: PMC9670005.
45. Lee H, Ozturk B, Stringer MS, Koundal S, MacIntosh BJ, Rothman D, et al. Choroid plexus tissue perfusion and blood to CSF barrier function in rats measured with continuous arterial spin labeling. *NeuroImage.* 2022; 261:119512. Epub 20220723. <https://doi.org/10.1016/j.neuroimage.2022.119512> PMID: 35882269; PubMed Central PMCID: PMC9969358.
46. Damkier HH, Brown PD, Praetorius J. Cerebrospinal fluid secretion by the choroid plexus. *Physiol Rev.* 2013; 93(4):1847–1892. <https://doi.org/10.1152/physrev.00004.2013> PMID: 24137023.
47. Lun MP, Monuki ES, Lehtinen MK. Development and functions of the choroid plexus-cerebrospinal fluid system. *Nat Rev Neurosci.* 2015; 16(8):445–57. Epub 20150715. <https://doi.org/10.1038/nrn3921> PMID: 26174708; PubMed Central PMCID: PMC4629451.
48. Kuleshov MV, Jones MR, Rouillard AD, Fernandez NF, Duan Q, Wang Z, et al. Enrichr: a comprehensive gene set enrichment analysis web server 2016 update. *Nucleic Acids Res.* 2016; 44(W1):W90–7. Epub 2016/05/05. <https://doi.org/10.1093/nar/gkw377> PMID: 27141961; PubMed Central PMCID: PMC4987924.
49. Merico D, Isserlin R, Stueker O, Emili A, Bader GD. Enrichment map: a network-based method for gene-set enrichment visualization and interpretation. *PLoS ONE.* 2010; 5(11):e13984. Epub 2010/11/19. <https://doi.org/10.1371/journal.pone.0013984> PMID: 21085593; PubMed Central PMCID: PMC2981572.
50. Voineagu I, Wang X, Johnston P, Lowe JK, Tian Y, Horvath S, et al. Transcriptomic analysis of autistic brain reveals convergent molecular pathology. *Nature.* 2011; 474(7351):380–384. <https://doi.org/10.1038/nature10110> PMID: 21614001; PubMed Central PMCID: PMC3607626.
51. Werling DM, Parikshak NN, Geschwind DH. Gene expression in human brain implicates sexually dimorphic pathways in autism spectrum disorders. *Nat Commun.* 2016; 7:10717. <https://doi.org/10.1038/ncomms10717> PMID: 26892004; PubMed Central PMCID: PMC4762891.
52. Kissel LT, Werling DM. Neural Transcriptomic Analysis of Sex Differences in Autism Spectrum Disorder: Current Insights and Future Directions. *Biol Psychiatry.* 2020. Epub 2021/02/09. <https://doi.org/10.1016/j.biopsych.2020.11.023> PMID: 33551190.
53. Gupta S, Ellis SE, Ashar FN, Moes A, Bader JS, Zhan J, et al. Transcriptome analysis reveals dysregulation of innate immune response genes and neuronal activity-dependent genes in autism. *Nat Commun.* 2014; 5:5748. Epub 2014/12/11. <https://doi.org/10.1038/ncomms6748> PMID: 25494366; PubMed Central PMCID: PMC4270294.
54. Parikshak NN, Swarup V, Belgard TG, Irimia M, Ramaswami G, Gandal MJ, et al. Genome-wide changes in lncRNA, splicing, and regional gene expression patterns in autism. *Nature.* 2016; 540(7633):423–7. Epub 2016/12/06. <https://doi.org/10.1038/nature20612> PMID: 27919067; PubMed Central PMCID: PMC7102905.
55. Velmeshev D, Schirmer L, Jung D, Haeussler M, Perez Y, Mayer S, et al. Single-cell genomics identifies cell type-specific molecular changes in autism. *Science.* 2019; 364(6441):685–9. Epub 2019/05/18. <https://doi.org/10.1126/science.aav8130> PMID: 31097668; PubMed Central PMCID: PMC678724.
56. Wöhr M, Schwarting RK. Affective communication in rodents: ultrasonic vocalizations as a tool for research on emotion and motivation. *Cell Tissue Res.* 2013; 354(1):81–97. <https://doi.org/10.1007/s00441-013-1607-9> PMID: 23576070.
57. Hebb AO, Cusimano MD. Idiopathic normal pressure hydrocephalus: a systematic review of diagnosis and outcome. *Neurosurgery.* 2001; 49(5):1166–84; discussion 84–6. <https://doi.org/10.1097/00006123-200111000-00028> PMID: 11846911.
58. Oliveira LM, Nitrini R, Roman GC. Normal-pressure hydrocephalus: A critical review. *Dement Neuropsychol.* 2019; 13(2):133–143. <https://doi.org/10.1590/1980-57642018dn13-020001> PMID: 31285787; PubMed Central PMCID: PMC6601311.

59. Brautigam K, Vakis A, Tsitsipanis C. Pathogenesis of idiopathic Normal Pressure Hydrocephalus: A review of knowledge. *J Clin Neurosci*. 2019; 61:10–3. Epub 20181106. <https://doi.org/10.1016/j.jocn.2018.10.147> PMID: 30409528.
60. Kumar V, Umair Z, Kumar S, Goutam RS, Park S, Kim J. The regulatory roles of motile cilia in CSF circulation and hydrocephalus. *Fluids Barriers CNS*. 2021; 18(1):31. Epub 20210707. <https://doi.org/10.1186/s12987-021-00265-0> PMID: 34233705; PubMed Central PMCID: PMC8261947.
61. Attwell D, Buchan AM, Charpak S, Lauritzen M, Macvicar BA, Newman EA. Glial and neuronal control of brain blood flow. *Nature*. 2010; 468(7321):232–243. <https://doi.org/10.1038/nature09613> PMID: 21068832; PubMed Central PMCID: PMC3206737.
62. Chung C, Shin W, Kim E. Early and Late Corrections in Mouse Models of Autism Spectrum Disorder. *Biol Psychiatry*. 2021. Epub 2021/09/25. <https://doi.org/10.1016/j.biopsych.2021.07.021> PMID: 34556257.
63. Hatakeyama E, Hayashi K. KATNAL1 is a more active and stable isoform of katanin, and is expressed dominantly in neurons. *Biochem Biophys Res Commun*. 2018; 507(1–4):389–94. Epub 20181115. <https://doi.org/10.1016/j.bbrc.2018.11.048> PMID: 30448058.
64. Banks G, Lassi G, Hoerder-Suabedissen A, Tinarelli F, Simon MM, Wilcox A, et al. A missense mutation in *Katnal1* underlies behavioural, neurological and ciliary anomalies. *Mol Psychiatry*. 2018; 23(3):713–22. Epub 20170404. <https://doi.org/10.1038/mp.2017.54> PMID: 28373692; PubMed Central PMCID: PMC5761721.
65. Bartholdi D, Stray-Pedersen A, Azzarello-Burri S, Kibaek M, Kirchoff M, Oneda B, et al. A newly recognized 13q12.3 microdeletion syndrome characterized by intellectual disability, microcephaly, and eczema/atopic dermatitis encompassing the *HMGB1* and *KATNAL1* genes. *Am J Med Genet A*. 2014; 164A(5):1277–83. Epub 20140324. <https://doi.org/10.1002/ajmg.a.36439> PMID: 24664804.
66. C Yuen RK, Merico D, Bookman M, Howe JL, Thiruvahindrapuram B, Patel RV, et al. Whole genome sequencing resource identifies 18 new candidate genes for autism spectrum disorder. *Nat Neurosci*. 2017; 20(4):602–11. Epub 2017/03/07. <https://doi.org/10.1038/nn.4524> PMID: 28263302; PubMed Central PMCID: PMC5501701.
67. Bourgeron T. From the genetic architecture to synaptic plasticity in autism spectrum disorder. *Nat Rev Neurosci*. 2015; 16(9):551–563. <https://doi.org/10.1038/nrn3992> PMID: 26289574.
68. Bagni C, Zukin RS. A Synaptic Perspective of Fragile X Syndrome and Autism Spectrum Disorders. *Neuron*. 2019; 101(6):1070–88. Epub 2019/03/22. <https://doi.org/10.1016/j.neuron.2019.02.041> PMID: 30897358.
69. Basilico B, Morandell J, Novarino G. Molecular mechanisms for targeted ASD treatments. *Curr Opin Genet Dev*. 2020; 65:126–37. Epub 2020/07/14. <https://doi.org/10.1016/j.gde.2020.06.004> PMID: 32659636.
70. Yan Z, Rein B. Mechanisms of synaptic transmission dysregulation in the prefrontal cortex: pathophysiological implications. *Mol Psychiatry*. 2021. Epub 2021/04/21. <https://doi.org/10.1038/s41380-021-01092-3> PMID: 33875802.
71. Qiu S, Cao H, Xue Y, Zhao W, Xie S, Wu N, et al. ASD mutation of *Katnal2* impairs ependymal ciliary motion and causes hydrocephalus. *bioRxiv*. 2023:2023.07.03.547302. <https://doi.org/10.1101/2023.07.03.547302>
72. Patro R, Duggal G, Love MI, Irizarry RA, Kingsford C. Salmon provides fast and bias-aware quantification of transcript expression. *Nat Methods*. 2017; 14(4):417–419. <https://doi.org/10.1038/nmeth.4197> PMID: 28263959; PubMed Central PMCID: PMC5600148.
73. Sonesson C, Love MI, Robinson MD. Differential analyses for RNA-seq: transcript-level estimates improve gene-level inferences. *F1000Res*. 2015; 4:1521. <https://doi.org/10.12688/f1000research.7563.2> PMID: 26925227; PubMed Central PMCID: PMC4712774.
74. Love MI, Huber W, Anders S. Moderated estimation of fold change and dispersion for RNA-seq data with DESeq2. *Genome Biol*. 2014; 15(12):550. <https://doi.org/10.1186/s13059-014-0550-8> PMID: 25516281; PubMed Central PMCID: PMC4302049.
75. Subramanian A, Kuehn H, Gould J, Tamayo P, Mesirov JP. GSEA-P: a desktop application for Gene Set Enrichment Analysis. *Bioinformatics*. 2007; 23(23):3251–3253. <https://doi.org/10.1093/bioinformatics/btm369> PMID: 17644558.
76. Subramanian A, Tamayo P, Mootha VK, Mukherjee S, Ebert BL, Gillette MA, et al. Gene set enrichment analysis: a knowledge-based approach for interpreting genome-wide expression profiles. *Proc Natl Acad Sci U S A*. 2005; 102(43):15545–15550. <https://doi.org/10.1073/pnas.0506580102> PMID: 16199517; PubMed Central PMCID: PMC1239896.
77. Isserlin R, Merico D, Voisin V, Bader GD. Enrichment Map—a Cytoscape app to visualize and explore OMICs pathway enrichment results. *F1000Res*. 2014; 3:141. Epub 2014/07/31. <https://doi.org/10.12688/f1000research.4536.1> PMID: 25075306; PubMed Central PMCID: PMC4103489.



78. Avants BB, Tustison NJ, Song G, Cook PA, Klein A, Gee JC. A reproducible evaluation of ANTs similarity metric performance in brain image registration. *NeuroImage*. 2011; 54(3):2033–44. Epub 20100917. <https://doi.org/10.1016/j.neuroimage.2010.09.025> PMID: 20851191; PubMed Central PMCID: PMC3065962.
79. Mirzadeh Z, Doetsch F, Sawamoto K, Wichterle H, Alvarez-Buylla A. The subventricular zone en-face: wholemount staining and ependymal flow. *J Vis Exp*. 2010; 39. Epub 20100506. <https://doi.org/10.3791/1938> PMID: 20461052; PubMed Central PMCID: PMC3144601.
80. Scattoni ML, Crawley J, Ricceri L. Ultrasonic vocalizations: a tool for behavioural phenotyping of mouse models of neurodevelopmental disorders. *Neurosci Biobehav Rev*. 2009; 33(4):508–515. <https://doi.org/10.1016/j.neubiorev.2008.08.003> PMID: 18771687; PubMed Central PMCID: PMC2688771.
81. Kim R, Kim J, Chung C, Ha S, Lee S, Lee E, et al. Cell-Type-Specific Shank2 Deletion in Mice Leads to Differential Synaptic and Behavioral Phenotypes. *J Neurosci*. 2018; 38(17):4076–4092. <https://doi.org/10.1523/JNEUROSCI.2684-17.2018> PMID: 29572432.